Coupled-channel analysis of high-energy electron scattering by ^{152}Sm and ^{166}Er*

L. S. Cardman, D. H. Dowell, R. L. Gulbranson, and D. G. Ravenhall

Physics Department, University of Illinois at Urbana-Champaign, Urbana, Illinois 61801

R. L. Mercer

IBM Watson Research Center, Yorktown Heights, New York 10598

A coupled-channel computer program has been used to calculate dispersion corrections to elastic and inelastic electron scattering from ^{152}Sm and ^{166}Er arising from the virtual excitation of some intermediate states in the ground state rotational band. Data from recent experiments on these nuclei have been analyzed using both phenomenological and Fourier-Bessel forms for the transition charge densities. The inclusion of dispersion corrections in the analysis was found to affect the extracted nuclear transition charge densities at a level comparable to other sources of uncertainty. These dispersion corrections did not remove the discrepancies existing between these experiments and the predictions of microscopic theories.

> NUCLEAR REACTIONS ^{152}Sm(e,e'), and ^{166}Er(e,e') calculations, coupled-chan-nels, 35 MeV $< E <$ 350 MeV. Dispersive effects on elastic and inelastic cross sec-tions and on extracted nuclear shapes.

I. INTRODUCTION

Electron scattering provides a precise probe for the investigation of charge and current densities for both the nuclear ground state and for transitions to higher states. This precision is due in part to the fact that the electron-nucleus interaction is electromagnetic in nature, and therefore calculable to high precision within the framework of quantum electrodynamics. Because the interaction is well understood, experiments can be interpreted unambiguously in terms of the nuclear structure. Present analysis techniques use numerical methods to calculate the distortion of the electron wave function by the Coulomb monopole field of the nucleus exactly. The transition potentials, however, are treated only to first order. While this approximation is generally quite good (because the transition potentials are relatively weak), the accuracy of modern electron-scattering experiments is increasing rapidly toward the point where higher-order effects will become important.

A large number of theoretical investigations have been carried out to examine the importance of higher-order (or dispersion) corrections in electron scattering.[1] The general conclusion to be drawn from these investigations is that dispersive effects are small, of order 10% in the region of the diffraction minima and less elsewhere. An exact treatment of the general problem of higher-order scattering is essentially impossible as one must include the excitation of all possible nuclear states. Previous authors have therefore employed a variety of approximations in order to arrive at a solution. These approximations have involved the choice of calculational techniques, the intermediate states included, the treatment of the transition potentials, and a variety of other considerations. Recently, Mercer and Ravenhall have constructed a computer code ZENITH,[2-4] which solves the problem with only two assumptions. First, they consider only a finite number of nuclear states, and second, they neglect the energy loss in inelastic scattering. All other details of the calculation, including the distortion of the electron wave function and the treatment of the multipole transition potentials, have been solved exactly through the use of numerical techniques.

Many authors have suggested that there are two main components to dispersive corrections in electron scattering. The first component, which comes from the excitation of intermediate states common to all nuclei (such as the giant collective states and the quasifree nucleon states), is expected to vary quite slowly and smoothly from nucleus to nucleus. The second component arises from the occurrence of low-lying excited states strongly coupled to the ground state in a manner varying from nucleus to nucleus. The virtual effect of these low-lying intermediate states may be substantial.

It is the aim of this work to examine quantitatively the level at which corrections of the second kind affect the extraction of nuclear transition charge densities from the experimental data. We have considered the cases of the rotational nuclei ^{152}Sm and ^{166}Er for three reasons. First, both of these nuclei have low-lying rotational bands

strongly coupled to the ground state. The neglect of energy loss in the scattering is an excellent approximation in this case. Second, data of excellent quality exist for these nuclei from recent experiments at Saclay[5] and MIT[6]. Finally, because the observed states are well-described by the rotational model, it is possible to predict with confidence for these nuclei those transition charge densities which are not accessible to measurement by electron scattering but which are required to calculate the dispersion correction accurately.

It must be recognized that the calculations we have undertaken, as outlined in Sec. II below, are incomplete in that we have included only a finite number of intermediate states. It is possible that some cancellation of the dispersion correction might result if all possible intermediate states were included. It is our belief, however, that, by including all known effects in this more limited system to an accuracy considerably greater than present experiments achieve, our calculations provide a more reliable guide to the magnitude of dispersive processes than has been available heretofore. Furthermore, by studying in considerable detail the manner in which the neglect of these processes affects the analysis of electron-scattering data, we have also determined the level of accuracy at which dispersive processes affect the nuclear structure information obtainable from these experiments. Details of the data-analysis procedures employed are presented in Sec. III, and the results of this analysis for electron scattering from the ground-state rotational band of ^{152}Sm are presented in Sec. IV. Results of a similar analysis for ^{166}Er are presented in Sec. V. Our conclusions regarding the importance of dispersive effects in this data are given in Sec. VI.

II. THEORY

A coupled-channel scheme has been employed to obtain some of the dispersive corrections to the customary partial wave (elastic) and distorted-wave Born approximation (DWBA) (inelastic) treatments of electron scattering. Its methods have been described in detail elsewhere[3] and the magnitude of the corrections it makes to cross sections have been illustrated in several cases.[2-4] For completeness, we discuss here the basic assumptions made, the physical couplings included, the degree of accuracy of the methods, and the physical processes not included. We shall not, however, repeat the computational details.

The only interaction included between the electron and the nucleus in the present calculations is the Coulomb potential of the nuclear charge distribution. For the excitation energies Δ involved (the largest, in ^{152}Sm, is 0.712 MeV), the effect of the transverse electric interaction with the nuclear current distribution (of relative order $(v/c)^2[\frac{1}{2} + \tan^2(\frac{1}{2}\theta)] \sim (\Delta/Mc^2[\frac{1}{2} + \tan^2(\frac{1}{2}\theta)]$ where M is the rotating mass of the nucleus) is small at all angles used ($\lesssim 10^{-4}$). Since the purpose of the coupled-channel calculation is to obtain the contributions of multiple interactions, which further accentuate the stronger couplings, this omission is not serious. In the coupled-channel program the nuclear excitation energies themselves are also neglected. The effect of this approximation has been examined in Ref. 2, where it is shown to vary as Δ/E, and to be negligible already at $E = 50$ MeV.

All allowed matrix elements of the nuclear charge density operator $\rho_{op}(\vec{r})$ can in principle contribute to the scattering via the Coulomb interaction. Between states $|nIM\rangle$ and $|n'I'M'\rangle$, the expansion

$$\langle n'I'M' | \rho_{op}(\vec{r}) | nIM\rangle$$

$$= \sqrt{4\pi} \sum_{lm} (-1)^m \langle IMlm|I'M'\rangle / (2I'+1)^{1/2}$$

$$\times i^l \rho_l^{n'n}(r) Y_{lm}(\Omega)$$

defines charge multipole radial matrix elements $\rho_l^{n'n}(r)$. Each $\rho_l^{n'n}(r)$ generates a Coulomb potential $\phi_l^{n'n}(r)$ of the same multipolarity l, which has the form

$$\phi_l^{n'n}(r) = 4\pi/(2l+1)\left[r^{-l-1} \int_0^r \rho_l^{n'n}(t)t^{l+2}dt \right.$$

$$\left. + r^l \int_r^\infty \rho_l^{n'n}(t)t^{1-l}dt \right].$$

The computer program works with matrix elements between states of total (electron + nucleus) angular momentum $\vec{F}$ of the potentials which are the sum of all such possible multipole contributions, indicated schematically for $l = 0$, 2, 4, and 6 in Fig. 1. In Fig. 1b, for example, are shown diagrammatically all possible quadrupole couplings among the $I = 0$, 2, 4, and 6 states with which the present analysis is concerned. It is clear that not all of the quantities $\rho_2^{n'n}(r)$ are accessible to experiment. In many cases the $B(E2;nn')$, measured by photon transitions, will give the overall normalization of $\rho_2(r)$ in the form $\int_0^\infty \rho_2^{n'n}(r)r^4dr$, but the scattering problem requires (to an extent depending on the maximum momentum transfer) the function $\rho_2^{n'n}(r)$ itself. It thus appears that for general l it is possible to make definite calculations only with a nuclear model which relates the unmeasurable $\rho_l^{n'n}(r)$ to quantities which are measurable. The model we have
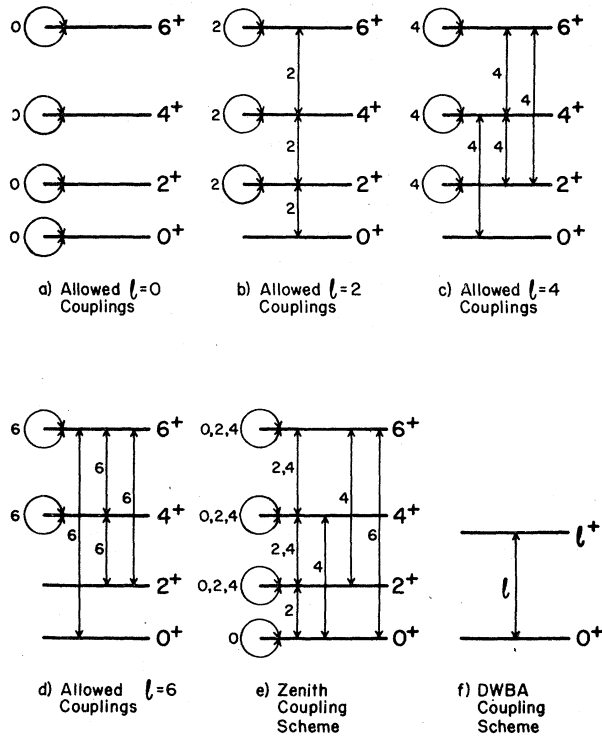
FIG. 1. (a) → (d) Allowed $l = 0$, 2, 4, and 6 couplings among the 0^+, 2^+, 4^+ and 6^+ levels in the ground-state rotational band. (e) The coupling scheme used in ZENITH for the ground-state rotational band. (f) The coupling scheme employed in the usual DWBA calculation for inelastic scattering to a level in the ground-state rotational band.

used for describing electron scattering from rotational nuclei follows the same assumptions as those of Bertozzi *et al.*[7]: (1) The nuclear Hamiltonian can be separated into a rotational Hamiltonian and an intrinsic Hamiltonian which describes all other degrees of freedom. (2) The nucleus has axial symmetry and reflection symmetry. Within the context of this rotational model, all transitions of a given multipolarity among states of the same rotational band have the same radial shape, and their normalizations, specified conveniently by their $B(El; nn')$, are all related. The rest of the present paper confines itself to this nuclear model.

The starting point of the coupled-channel calculations is therefore the charge distribution $\rho(\vec{r})$ of the nucleus in its intrinsic frame, expanded into multipoles:

$$\rho(\vec{r}) = \sqrt{4\pi} \sum_l \rho_l(r) Y_{l\,0}(\Omega) . \tag{1}$$

Two approaches have been taken to the problem of extracting the intrinsic nuclear shape $\rho(\vec{r})$. In the

first, $\rho(\vec{r})$ itself is parametrized and the various $\rho_l(r)$ are projected numerically using the relationship

$$\rho_l(r) = \frac{1}{\sqrt{4\pi}} \int \rho(\vec{r}) Y_{l\,0}(\Omega) d\Omega , \tag{2}$$

and are determined by simultaneously fitting the scattering data from all levels observed. In the second approach, for greater flexibility the individual $\rho_l(r)$ are determined separately, from independent fits to the scattering from each level. In this case, Eq. (1) then serves to define $\rho(\vec{r})$. The details of these procedures are described in the next section. Specification of these functions, and consequently of the moments which determine their normalization, such as the intrinsic quadrupole moment,

$$Q_0 = (16\pi/5)^{1/2} M(E2, 0) ,$$

where

$$M(El, \mu) = \int \rho(\vec{r}) r^l Y_{l\mu}(\Omega) d^3r ,$$

completely determines the multipole transition charge densities $\rho_l^{n'n}(r)$. As has been described in Ref. 3, the radial shapes of $\rho_l(r)$ and $\rho_l^{n'n}(r)$ are identical, and the strength $S_l^{n'n}$ which defines the asymptotic behavior of $\phi_l^{n'n}(r)$ by $e\phi_l^{n'n}(r)$ $\sim S_l^{n'n}/r^{l+1}$, is given by

$$S_l^{n'n} = 4\pi e \left[(2I+1)/(2l+1) \right]^{1/2} i^{I-I-I'} \langle IOlO | I'O \rangle$$

$$\times \int_0^\infty \rho_l(r) r^{l+2} dr , \tag{3}$$

where $\rho_0(r)$ is normalized as defined in Eq. (1). The $B(El, n \to n')$ associated with the transition from a 0^+ ground state is then given by

$$B(El, n \to n') = \frac{(2l+1)}{4\pi} \left[\frac{S_l^{n'n}}{e} \right]^2 \tag{4}$$

and the transition radius $R_{tr}|_l$ by

$$R_{tr}|_l = \left[\int_0^\infty \rho_l(r) r^{l+2} r^2 dr \Big/ \int_0^\infty \rho_l(r) r^l r^2 dr \right]^{1/2} . \tag{5}$$

The couplings included in the present calculation, shown in Fig. 1e, are those of Figs. 1a, 1b, and 1c, with only the $0^+ \to 6^+$ contribution of $l = 6$ included from Fig. 1d. From this point, with appropriately chosen computational parameters, the program ZENITH determines the elastic and inelastic differential cross sections resulting from the coupling scheme assumed. Adjustable parameters such as the integration step size ΔR for inner integration, and the radius R_{max} assumed to contain all charge distributions, have been chosen conservatively. The one limiting quantity whose effect needed some later manual smoothing was the

number of F states (effectively the number of partial waves) used and its effect on the $0^+ \to 2^+$ inelastic cross section. The problem arises because of the quadrupole potential, the least rapidly decreasing of the coupling potentials, and is due to its diagonal contribution in the 2^+ state. The results quoted include states up to $F = 127/2$, i.e., about 60 partial waves. By varying the cutoff value, it is determined that after smoothing, the resulting corrections are known to about 0.1%, which is completely adequate for the present analysis.

The effect of the channel couplings included is specified to the data-analysis procedure in the form of ratios to one-channel elastic or DWBA inelastic cross sections. To avoid extraneous numerical errors, these comparison cross sections are also determined using ZENITH under the same computational conditons. The coupling scheme for the DWBA simulation is that of Fig. 1f, and in the case $l = 2$, where the actual excitation strength is large enough that higher-order effects would be included also, the strength S_2^{01} is reduced by $\sqrt{10}$, and the resulting cross sections multiplied by 10.

The set of physical processes and couplings which are beyond the capabilities of the present analysis, but which might make appreciable contributions, involve the higher-lying collective nuclear states. These lie too high in energy for the present treatment, which must assume zero excitation energy, to be reliable. They would also involve an impractically large number of coupled states. The physical situation to which the present methods are directed assumes that only the low-lying states affect each other intimately, so that all couplings need individual specification, while the high-lying collective states have a smoother, more averaged effect. These extra contributions, ignored at present, might then be included in terms either of optical potential contributions to the potential for each state, or by suitable redefinition of effective charge densities. These matters are under active investigation, by us and other workers.

III. DATA-ANALYSIS PROCEDURES

A. DWBA fits to the data using analytic charge densities

Initial fits to the data were performed using the computer code DEFFIT.[8] In this code the ground-state and transition charge densities are obtained from parameterized, phenomenological shapes, and the best-fit values for these parameters are obtained using the usual nonlinear least squares technique.[9] The criterion for a

best-fit is the minimization of χ^2 where

$$\chi^2 = \sum_{i=1}^{N} \left[\frac{(\sigma_i^t - \sigma_i^e)}{\Delta \sigma_i^e} \right]^2 . \tag{6}$$

The quantities N, σ_i^t, σ_i^e, and $\Delta \sigma_i^e$ represent the number of data points, the ith theoretical cross section, the ith experimental cross section, and the statistical error in σ_i^e respectively. The theoretical cross sections are calculated from the relevant charge density using a modified version of the DWBA code HEINEL.[10] For fitting rotational nucleus data, DEFFIT has two modes of analysis. In the first mode, it is assumed that all of the observed states are characterized by rigid rotation of a single, simply parametrized intrinsic nuclear shape. Therefore, the cross sections for all of the levels observed are included in the χ^2 sum and the best-fit shape is taken to be that intrinsic shape which minimizes the total χ^2 summed over all levels observed. In its second mode of fitting, DEFFIT treats the scattering to each nuclear state independently and finds the best-fit transition charge density for each level separately. The corresponding intrinsic shape is then obtained via Eq. (1). This technique provides degrees of flexibility not available in the first fitting mode.

Within the context of the rigid rotor model, we have considered two parametrized shapes for the intrinsic charge distribution. They are the following:

The deformed Fermi distribution (DF)

$$\rho(r, \theta) = \rho_0 \frac{1 + w \left[\dfrac{r}{c(\theta)} \right]^2}{1 + \exp \left[\dfrac{r - c(\theta)}{z} \right]}, \tag{7}$$

where

$$c(\theta) = c_0 \left[1 + \beta_2 Y_{20}(\theta) + \beta_4 Y_{40}(\theta) + \beta_6 Y_{60}(\theta) \right] ,$$

and the deformed modified Gaussian distribution (DMG)

$$\rho(r, \theta) = \frac{1 + w \left[\dfrac{r}{c(\theta)} \right]^2}{1 + \exp \left[\dfrac{r^2 - c^2(\theta)}{z^2} \right]}, \tag{8}$$

where

$$c^2(\theta) = c_0^2 \left[1 + \beta_2 Y_{20}(\theta) + \beta_4 Y_{40}(\theta) + \beta_6 Y_{60}(\theta) \right] .$$

In the first mode of fitting, DEFFIT uses one of the shapes described above, together with Eq. (2) to generate the transition charges used in the calculation of the cross sections, for all of the levels observed, based on a single parameter set $\{ c_0, z, w, \beta_2, \beta_4, \beta_6 \}$. In the second (separated fit) mode, independent parameter sets $\{ c_0, z, w, \beta_2, \beta_4,$

$\beta_6\}_l$ are used in one of the shapes above for the calculation of the scattering for each multipole l, and the resultant independent transition charges are combined to yield the intrinsic shape of the nucleus using the relationship of Eq. (1).

In addition to nonlinear least squares fitting of elastic and inelastic cross sections, DEFFIT can also do constrained nonlinear least squares fitting. The rms radius of the ground state charge density and/or the $B(E2)$ of the first excited state can be entered as data points with errors, and the χ^2 sum of Eq. (6) is augmented appropriately during fitting. Using this technique, it is further possible to rigidly constrain the fits to an input rms radius and/or $B(E2)$ by using unrealistically small error bars for these quantities. These constraints are essential for the analysis of low-energy experiments where the momentum transfer region covered is too small to permit determination of all of the model parameters from the electron-scattering data alone. The constraints can also be used in the analysis of high-q data to improve our knowledge of the radial behavior of the relevant charge densities.

The program DEFFIT determines uncertainties in the best-fit parameters in the usual way. Defining the curvature matrix $\underline{\alpha}$ by

$$\alpha_{ij} = \frac{1}{2}\frac{\partial^2\chi^2}{\partial p_i \partial p_j} \cong \sum_{k=1}^{N}\left[\frac{1}{(\Delta\sigma_k^e)^2}\frac{\partial \sigma_k^t}{\partial p_i}\frac{\partial \sigma_k^t}{\partial p_j}\right],$$

where p_i and p_j are the ith and jth parameters of the charge density model under consideration, and the partial derivatives are evaluated at the minimum of χ^2, then the error matrix $\underline{\epsilon} = \underline{\alpha}^{-1}$, and the uncertainty Δp_i in the parameter p_i is given by

$$\Delta p_i = \sqrt{\epsilon_{ii}} \ .$$

This is the maximum uncorrelated change in p_i which results in the total χ^2 increasing by one. The error matrix is also used to propagate parameter uncertainties to determine the uncertainty in quantities Q, such as the rms radius, which are functions of the parameters through use of the relationship

$$\Delta Q^2 = \sum_i \sum_j \epsilon_{ij}\frac{\partial Q}{\partial p_i}\frac{\partial Q}{\partial p_j} \ .$$

The final consideration in DWBA fitting was the conversion of cross sections measured at different energies to cross sections at a common energy. This was desirable because the execution time of the DWBA code HEINEL depends primarily on the number of incident energies considered. Each cross section $\sigma_i(E_i, \theta_i)$ measured at the energy and angle E_i, θ_i was transformed to the common energy E_0 by first choosing an angle θ_i' such that the effective momentum transfers q_{eff}

for both combinations of energy and angle are equal:

$$q_{eff}(E_0, \theta_i') = q_{eff}(E_i, \theta_i) \ ,$$

where

$$q_{eff}(E, \theta) = q(E, \theta)\left(1 + \frac{Ze^2}{R_{tr}|_l E_0}\right) , \qquad (9)$$

$$q(E, \theta) = \frac{2E\sin(\theta/2)}{\hbar c} \ ,$$

and $R_{tr}|_l$ is the appropriate transition radius as given by Eq. (5). After choice of the angle θ_i', the cross section was then transformed using

$$\sigma_i(E_0, \theta_i') = T\sigma_i(E_i, \theta_i)$$

where T is the ratio of theoretical cross sections calculated using HEINEL at (E_0, θ_i') and (E_i, θ_i), respectively. The correctness of this transform depends on our knowledge of the appropriate transition charge, which of course is to be determined from a fit to the transformed cross sections. It was therefore necessary to use an iterative procedure whereby after each nonlinear least squares fit the transformation factors T are recalculated using the new best-fit transition charge. Three iterations of this procedure were adequate in all cases for the process to have converged to within $\frac{1}{20}$ of the corresponding experimental cross section uncertainties.

B. DWBA fits to the data using Fourier-Bessel charge densities

In recent years several techniques have been developed for the analysis of elastic and inelastic electron-scattering data with the aim of deducing the ground-state and transition charge densities without the constraints imposed by the assumption of phenomenological forms. The most popular of these techniques are the "sum of Gaussians" method of Sick[11] and the Fourier-Bessel expansions of Dreher et al.,[12,13] and Friar and Negele.[14] We have analyzed the scattering data for ^{152}Sm and ^{166}Er using the second of these techniques in an effort to obtain a less model-dependent description of the effect of the inclusion of coupled-channel corrections in the data analysis. Following Dreher et al.,[12,13] we assume that the transition charge density $\rho_l(r)$ for excitation of the lth multipole is restricted to a region $r < R$ and may be expanded into a Fourier-Bessel series using the spherical Bessel function j_l of order l:

$$\rho_l(r) = \begin{cases} \sum_{\nu=1}^{\infty} a_{l\nu}j_l(q_{l\nu}r), & r \leq R \\ 0, & r > R \end{cases} , \qquad (10)$$

where $q_{l\nu}$ is related to the νth zero of the lth spherical Bessel function: $j_l(q_{l\nu}R) = 0$. These

spherical Bessel functions form a complete set, and can therefore be used, in principle, to represent an arbitrary charge density in the region 0 to R. However, as has been pointed out by Borysowicz and Hetherington,[15] electron-scattering data cover only a limited range of momentum transfer, and lack of data beyond a maximum momentum transfer q_{max} restricts the extraction of the coefficients of the series describing the charge density [Eq. (10)] to $\nu \lesssim M$, where $q_{1M} \approx q_{max}$. Therefore, the determination of the complete set of coefficients $\{a_{l\nu}\}$ describing the lth transition charge requires that assumptions be made about the behavior of the experimental form factors beyond the region of measurement. In a manner similar to Borysowicz and Hetherington,[15] we added fictitious data at $q > q_{max}$ to the set under analysis. These data were generated for values $q_i^{fict} = q_{in}$, where $n = M + i$ and the form factors at these q_i^{fict} are taken to be $\frac{1}{2}$ the value of the envelope of the measured form factor projected to the momentum q_i^{fict}. The uncertainty in these fictitious cross sections were taken to be equal to their value. Three fictitious data points generated in this manner were added to each data set. To avoid pathological fits due to the location of these q_i^{fict} at the exact values q_{in}, it was necessary to include additional fictitious data points at momentum transfers uniformly spaced between the q_i^{fict}. Thus a total of six data points describing the envelope of the expected high-q behavior of the form factor were added to each data set. Starting values for the $a_{l\nu}$ were obtained by analytically expanding the best-fit phenomenological transition charge densities using Eq. (10).

For the high-q ^{152}Sm and ^{166}Er data analyzed, the number of parameters M determined directly from the data with a choice of 11 fm for the expansion radius R varied from nine for elastic scattering to six for the $l = 6$ inelastic scattering. The addition of fictitious cross sections beyond q_{max} was found to primarily affect the error band associated with $\rho_l(r)$. The effect on the values of the integral quantities, $B(El)$ and R_{tr}, was only at the level of a fraction of a standard deviation. The reason for this can be understood simply if we expand, for example, Eq. (4) in terms of Eq. (10). As shown in Ref. 13, $B(El)$ can then be written as

$$B(El) = 4\pi \left[R^{l+3} \sum_\nu \frac{a_{l\nu} j_{l+1}(q_{l\nu}R)}{q_{l\nu}R} \right]^2 .$$

Numerical analysis of the ^{152}Sm and ^{166}Er inelastic form factor best-fit coefficients shows for the $l = 2$ fits, for example, that only the first five or six terms contribute significantly to the sum above. Since the data determine the first eight coefficients in this case, the integral quantities are in-

sensitive to reasonable assumptions about the high-q behavior.

Several authors have considered in detail the effects of normalization errors, assumptions about high-q behavior of the form factor, completeness errors, and choice of basis sets on the "model-independent" analysis of electron-scattering data. We have restricted our attention primarily to the use of this technique for the determination of the changes in the extracted transition-charge densities, strengths, and radii due to the inclusion of coupled-channel effects in the analysis. As these changes should be far less sensitive than the quantities themselves to the assumptions and errors mentioned above, we have not examined their effect in detail. Our choice of high-q behavior determination is similar to that of Borysowicz and Hetherington.[15] These authors have also shown that the errors due to the choice of basis set are small, so we have neglected this source of uncertainty. Following Neuhausen,[16] we first analyzed the data including $M + 3$ terms in the sum of Eq. (8) and extracted the best-fit parameter set. We then fixed the $a_{l\nu}$ for $\nu > M + 1$ to the values obtained from the first fit, and recalculated the error matrix. This new error matrix was used to extract the uncertainties in the transition charge density and in the associated $B(El)$ and R_{tr}. As has been noted by other authors,[17] the use of a fit including only one term beyond the number determined directly from the data as an estimate of the completeness error is reasonable, but it is by no means definitive. We have also ignored as small, uncertainties due to the absolute normalization of the data. Such errors have been observed[16] to scale $B(El)$ directly, but to have little effect on the radial dependence of $\rho_l(r)$ or on R_{tr}. The procedure outlined above has been tested by applying it to the ^{64}Zn inelastic scattering results of Neuhausen. The extracted charge densities and uncertainties are in excellent agreement with his published results.[16]

Fourier-Bessel analysis of the elastic- and inelastic-scattering data was performed using the code SESFIT written at Illinois. In this code, nonlinear least squares techniques are used to fit the data in a manner similar to the DWBA fits described in Sec. III A above. Cross sections were calculated from nuclear charge densities given by Eq. (8) using the computer code HEINEL and the parameter set $\{a_{l\nu}\}_{\nu = 1, M+3}$ was found which minimized χ^2. Inelastic scattering to each member of the ground-state band was considered separately, and the resultant best-fit $\rho_l(r)$ were combined using Eq. (1) to determine the intrinsic nuclear shape. An energy renormalization technique identical to that employed in the model-dependent fits was used

to reduce the computation time required. The elastic-scattering fits included the constraint that the integral of the charge density yield the total nuclear charge Z.

C. Coupled-channel fits to the data

In principle, coupled-channel fits to the data could be obtained by simply inserting the code ZENITH in place of the code HEINEL in the nonlinear least squares programs described above. Unfortunately, ZENITH requires execution times orders of magnitude larger than HEINEL, and this approach is not practicable. The procedure we adopted is as follows. First, a DWBA analysis was performed of the experimental cross sections and best-fit ground-state and transition charge densities were extracted. These best-fit densities were then used as input to the code ZENITH, which calculated theoretical cross sections in both DWBA (σ_{DWBA}) and in the coupled-channel mode (σ_{CC}) in which couplings of all levels observed ($0^+, 2^+, 4^+, 6^+$) were considered. The results of these calculations were then used to determine correction factors F

$$F(E_i, \theta_i) = \frac{\sigma_{CC}(E_i, \theta_i)}{\sigma_{DWBA}(E_i, \theta_i)} - 1 , \qquad (11)$$

which transformed the measured cross sections $\sigma_i(E_i, \theta_i)$ to those that would have been measured if dispersive processes (as calculated by ZENITH) were not present in nature:

$$\sigma_i'(E_i, \theta_i) = \frac{\sigma_i(E_i, \theta_i)}{1 + F(E_i, \theta_i)} . \qquad (12)$$

These dispersion-corrected cross sections σ_i' were then fitted using the conventional DWBA analyses described above.

Because the corrected cross sections yield different best-fit transition charge densities, one should, in principle, iterate the correction of Eq. (12) and the subsequent DWBA fit using the new best-fit transition charges until a self-consistent set of cross sections, transition charges, and correction factors is determined. It was found, however, that the differences between the best-fit transition charges were sufficiently small that no iteration was required. Finally, it should be noted that the correction factors F are functions of both the incident energy and the momentum transfer. Because of this fact, the inclusion of coupled-channel effects in the analysis of data taken at different energies (as is the case for the [166]Er data) rather than at different angles but a fixed energy (as is the case for the [152]Sm data) requires considerably more computational effort. Experimentalists

wishing to improve the accuracy of their data analysis might keep this fact in mind.

IV. ANALYSIS OF [152]Sm DATA

A. Saclay high-energy data

The first data analyzed were the results obtained by the Saclay-Tel-Aviv collaboration[5] on the scattering of 251.5 MeV electrons by [152]Sm. These data were initially analyzed in DWBA using a deformed Fermi distribution for the intrinsic nuclear shape. In this fit, as in all fits to the [152]Sm high-q data, the rms radius and its uncertainty as obtained from muonic x-ray studies was added as

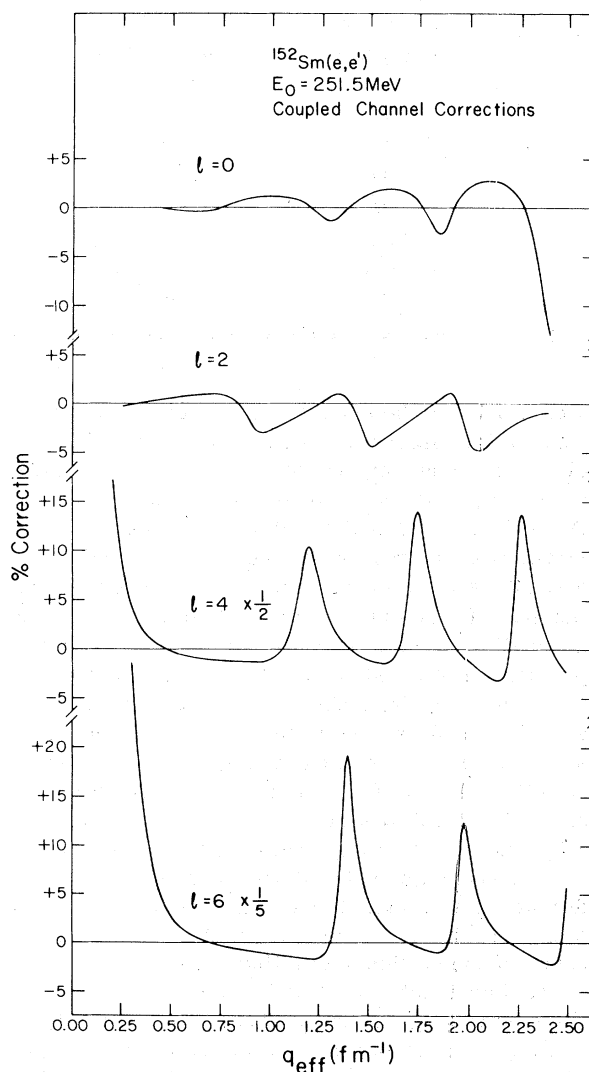FIG. 2. Coupled-channel dispersion corrections, in percent, for the $l = 0$, 2, 4, and 6 transitions in [152]Sm, including all couplings shown in Fig. 1(e). The correction is defined by Eq. (11).

TABLE I. Saclay 251.5 MeV ^{152}Sm data: deformed Fermi distribution fits. $\langle r^2 \rangle^{1/2}$ was constrained by adding the rms radius as a data point in the fit, $\langle r^2 \rangle^{1/2}_{const} = 5.085 \pm 0.06$ fm.

Parameter	DWBA analysis	Coupled-channel analysis	% dif.	dif./error
c_0 (fm)	5.7752 ± 0.0083	5.7714 ± 0.0084	$+0.07$	$+0.5$
z (fm)	0.5501 ± 0.0034	0.5515 ± 0.0035	-0.25	-0.4
β_2	0.2888 ± 0.0023	0.2895 ± 0.0023	-0.24	-0.3
β_4	0.0881 ± 0.0017	0.0885 ± 0.0017	-0.45	-0.2
β_6	0.0168 ± 0.0015	0.0180 ± 0.0016	-6.67	-0.8
$\langle r^2 \rangle^{1/2}$ (fm)	5.0316 ± 0.0042	5.0316 ± 0.0043	0.00	0
$R_{tr}\vert_2$ (fm)	6.9067 ± 0.0073	6.9091 ± 0.0074	-0.03	-0.3
$R_{tr}\vert_4$ (fm)	7.6680 ± 0.0116	7.6736 ± 0.0116	-0.07	-0.5
$R_{tr}\vert_6$ (fm)	8.3601 ± 0.0170	8.3583 ± 0.0169	$+0.02$	$+0.1$
$B(E2)$ (e^2b^2)	3.518 ± 0.058	3.536 ± 0.0579	-0.51	-0.3
$B(E4)$ (e^2b^4)	0.2101 ± 0.0061	0.2131 ± 0.0062	-1.41	-0.5
$B(E6)$ (e^2b^6)	0.0141 ± 0.0008	0.0148 ± 0.0009	-4.73	-0.8
χ^2_0	56	53		
χ^2_2	45	46		
χ^2_4	65	53		
χ^2_6	7	8		
$\chi^2_{constraints}$	0.8	0.8		
χ^2_{total}	174	161		
ν	67	67		

a data point in the elastic-scattering fit. The results of this analysis, which are presented in Table I, are in agreement with the results of Nakada et al.,[5] with the exception of the $l = 6$ transition. Our values for β_6 and $B(E6)$ are substantially larger than the values obtained by these authors, a result which we believe is due to unequal weighting given to the elastic data in their fit. The overall quality of our fit is reasonably good, with χ^2 per degree of freedom ν on the order of 2.6.

The nuclear shape obtained from this DWBA fit was then used as input to ZENITH, and the dispersion correction F was calculated as described in Sec. III C above. The results of this calculation, shown in Fig. 2, display many features common to all of our calculations. The correction is largest (as a percentage of the DWBA cross section) in the diffraction minima. For elastic scattering it goes to zero in the forward direction due to the dominance of the Coulomb amplitude at low q. In marked contrast, the 4^+ and 6^+ corrections become quite large at low q. This is due to the fact that a q^{2l-4} dependence is predicted for the cross section for excitation of the lth multipole in DWBA. The $l = 4$ and 6 cross sections are therefore proportional to q^4 and q^8, respectively. The dispersion correction, however, is dominated at low q

by sequential excitations which are mediated by quadrupole potentials, and thus are proportional to q^0 in the forward direction. This results in a very large percentage correction. For the $l = 2$ excitation, the correction remains small in the forward direction because the DWBA cross section itself is also proportional to q^0. Finally, it should be noted that the correction does not go to zero outside the diffraction minima, in contrast to the results of several other calculations,[1] but rather is a gradual function of q_{eff} which varies from multipole to multipole and nucleus to nucleus. This implies that attempts to remove dispersive effects from electron-scattering experiments by simply excluding data in the diffraction minima from the analysis will not be successful.

The correction factors F were used to remove coupled-channel effects from the measured cross sections as described in Sec. III C above, and the resulting cross sections were refit. The results of this coupled-channel fit are shown in Fig. 3, and the new parameter set extracted is shown in Table I. As is evident from this table, the inclusion of coupled-channel effects in the analysis modified the deduced nuclear shape only very slightly. None of the charge-distribution parameters varied by as much as one standard deviation
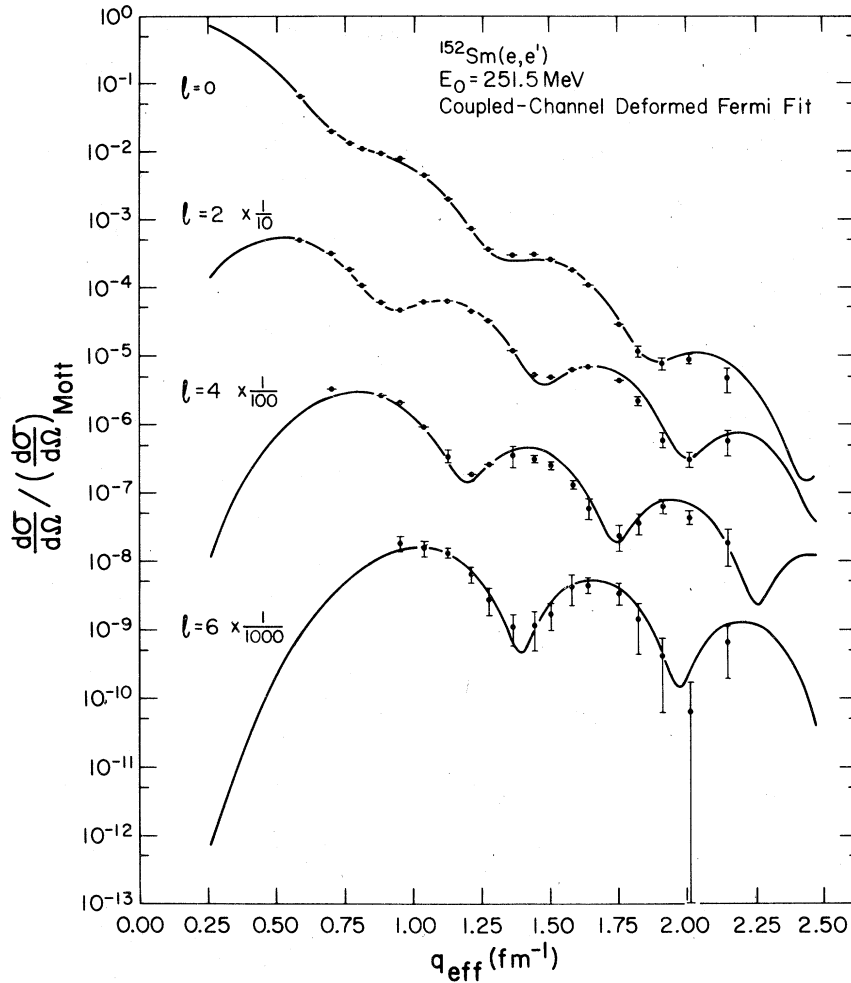
FIG. 3. Experimental form factors (corrected for coupled-channel effects) for elastic ($l = 0$) and inelastic ($l = 2$, 4, and 6) scattering from ^{152}Sm as measured in the Saclay high-energy experiment (Ref. 5). The solid curves are based on the best-fit deformed Fermi charge distribution.

from the value obtained by the DWBA fit. At first glance this would seem surprising in light of the large corrections to the cross sections. However, inspection of the experimental cross sections reveals that the magnitude of the cross-section uncertainty is typically similar to the magnitude of the dispersion correction. This fact significantly reduces the impact of the coupled-channel corrections on the deduced shape for this data.

A similar procedure was followed in analyzing this data using a deformed modified Gaussian distribution for the intrinsic nuclear shape. The results of these fits were qualitatively similar to the results of the deformed Fermi distribution fits in that the inclusion of coupled-channel effects yielded changes of less than one standard deviation for all parameters. The overall quality of the fit was,

however, significantly worse, with χ^2/ν equal to 268/66. As will be seen, the relatively poor χ^2 obtained in both of these simple intrinsic shape fits is due to restrictions contained in the nuclear models employed, rather than to the quality of the experimental data.

The third "model-dependent" fit to the high-q ^{152}Sm data was made using the separated deformed Fermi (SDF) distribution. In this model, the parameters c_0, z, and β_l were determined independently for each multipole l, and the intrinsic shape was then obtained via Eq. 1. Because the fits to each form factor are uncoupled, this model has considerably more freedom to respond to changes in the cross sections due to the inclusion of coupled-channel effects, and should therefore be more sensitive to their presence. The results of these

TABLE II. Saclay 251.5 MeV ^{152}Sm data: separated deformed Fermi distribution fits. $\langle r^2 \rangle^{1/2}$ was constrained by adding the rms radius as a data point in the $l=0$ fit, $\langle r^2 \rangle^{1/2}_{const} = 5.085 \pm 0.06$ fm.

	Parameter	DWBA analysis	Coupled-channel analysis	% dif.	dif./error
	c_0 (fm)	5.8142 ± 0.0171	5.8136 ± 0.0189	$+0.01$	0
	z (fm)	0.5005 ± 0.0263	0.4940 ± 0.0293	$+1.32$	$+0.2$
$l=0$	β_2	0.3320 ± 0.0266	0.3439 ± 0.0351	-3.46	-0.3
	β_4	0.0881 [a]	0.0881 [a]		
	β_6	0.0168 [a]	0.0168 [a]		
	$\langle r^2 \rangle^{1/2}$ (fm)	5.0237 ± 0.0051	5.0249 ± 0.0065	-0.02	-0.2
	χ^2/ν	$42/16$	$42/16$		
	c_0 (fm)	5.7555 ± 0.0172	5.7697 ± 0.0174	-0.25	-0.8
	z (fm)	0.5866 ± 0.0084	0.5850 ± 0.0085	$+0.27$	$+0.2$
$l=2$	β_2	0.3100 ± 0.0047	0.3116 ± 0.0048	-0.51	-0.3
	β_4	0.0881 [a]	0.0881 [a]		
	β_6	0.0168 [a]	0.0168 [a]		
	$R_{tr}|_2$ (fm)	7.0005 ± 0.0250	7.0119 ± 0.0252	-0.16	-0.5
	$B(E2)$ $(e^2 b^2)$	4.119 ± 0.151	4.203 ± 0.155	-2.00	-0.5
	χ^2/ν	$21/17$	$21/17$		
	c_0 (fm)	5.8797 ± 0.0285	5.8439 ± 0.0284	$+0.61$	$+1.3$
	z (fm)	0.6095 ± 0.0132	0.6164 ± 0.0133	-1.12	-0.5
$l=4$	β_2	0.2888 [a]	0.2888 [a]		
	β_4	0.1040 ± 0.0030	0.1038 ± 0.0030	$+0.19$	$+0.1$
	β_6	0.0168 [a]	0.0168 [a]		
	$R_{tr}|_4$ (fm)	7.9732 ± 0.0501	7.9630 ± 0.0516	$+0.13$	$+0.2$
	$B(E4)$ $(e^2 b^4)$	0.3319 ± 0.0241	0.3204 ± 0.0236	$+3.59$	$+0.5$
	χ^2/ν	$17/14$	$9/14$		
	c_0 (fm)	5.7809 ± 0.0682	5.7575 ± 0.0633	$+0.41$	$+0.4$
	z (fm)	0.5951 ± 0.0297	0.6022 ± 0.0296	-1.18	-0.2
$l=6$	β_2	0.2888 [a]	0.2888 [a]		
	β_4	0.0881 [a]	0.0881 [a]		
	β_6	0.0184 ± 0.0023	0.0195 ± 0.0024	-5.64	-0.5
	$R_{tr}|_6$ (fm)	8.5648 ± 0.1573	8.5703 ± 0.1597	-0.06	0
	$B(E6)$ $(e^2 b^6)$	0.0171 ± 0.0038	0.0174 ± 0.0039	-1.72	-0.1
	χ^2/ν	$4/12$	$3/12$		

[a]Not varied during fit.

fits, shown in Table II, indicate once again that the effect of coupled-channel corrections on the deduced nuclear shape is quite small for ^{152}Sm. The quality of the fits is significantly better than was obtained using either of the simple rigid rotation models, with χ^2/ν of order one for all levels except the ground state. A careful examination of the results of the SDF distribution fits provides insight into the difficulties encountered in either of the earlier model fits to the ^{152}Sm data. As can be seen from Table II, when the length parameter c_0 is allowed to vary independently for

each excitation, the resultant best-fit values are different for each multipole, whereas in the simple intrinsic shape fits, c_0 is restricted to the same value for all multipoles.

The final model-dependent fits to the data, obtained using the separated deformed modified Gaussian (SDMG) distribution, are shown in Table III. This distribution yielded the best model fits for ^{152}Sm, with χ^2/ν of order one for all levels. As was the case for the SDF distribution fits, the best-fit length parameter c_0 was different for each level. Inclusion of coupled-channel effects

TABLE III. Saclay 251.5 MeV ^{152}Sm data: separated deformed modified Gaussian distribution fits. $\langle r^2 \rangle^{1/2}$ was constrained by adding the rms radius as a data point in the $l = 0$ fit, $\langle r^2 \rangle^{1/2}_{\text{const}} = 5.085 \pm 0.06$ fm.

	Parameter	DWBA analysis	Coupled-channel analysis	% dif.	dif./error
$l = 0$	c_0 (fm)	5.8936 ± 0.0155	5.8913 ± 0.0155	$+0.04$	$+0.2$
	z (fm)	2.1393 ± 0.0540	2.1521 ± 0.0542	-0.59	-0.2
	w	0.0381 [a]	0.0315 [a]		
	β_2	0.9333 ± 0.0199	0.9319 ± 0.0203	$+0.15$	$+0.1$
	β_4	0.1932 [a]	0.1944 [a]		
	β_6	0.0428 [a]	0.0448 [a]		
	$\langle r^2 \rangle^{1/2}$ (fm)	4.9949 ± 0.0050	4.9942 ± 0.0050	$+0.01$	$+0.1$
	χ^2/ν	$10/16$	$11/16$		
$l = 2$	c_0 (fm)	5.8193 ± 0.0156	5.8335 ± 0.0156	-0.24	-0.9
	z (fm)	2.7011 ± 0.0196	2.7007 ± 0.0193	$+0.01$	0.0
	w	0.0381 [a]	0.0315 [a]		
	β_2	0.6433 ± 0.0097	0.6463 ± 0.0097	-0.46	-0.3
	β_4	0.1932 [a]	0.1944 [a]		
	β_6	0.0428 [a]	0.0448 [a]		
	$R_{\text{tr}}|_2$ (fm)	6.7530 ± 0.0191	6.7651 ± 0.0193	-0.18	-0.6
	$B(E2)$ (e^2b^2)	3.479 ± 0.113	3.554 ± 0.116	-2.11	-0.7
	χ^2/ν	$25/17$	$25/17$		
$l = 4$	c_0 (fm)	5.9739 ± 0.0288	5.9381 ± 0.0282	$+0.60$	$+1.3$
	z (fm)	2.8629 ± 0.0308	2.8719 ± 0.0308	-0.31	-0.3
	w	0.0381 [a]	0.0315 [a]		
	β_2	0.6130 [a]	0.6139 [a]		
	β_4	0.2323 ± 0.0059	0.2313 ± 0.0059	$+0.43$	$+0.2$
	β_6	0.0428 [a]	0.0448 [a]		
	$R_{\text{tr}}|_4$ (fm)	7.6449 ± 0.0353	7.6227 ± 0.0358	$+0.29$	$+0.6$
	$B(E4)$ (e^2b^4)	0.2501 ± 0.0163	0.2394 ± 0.0155	$+4.47$	$+0.7$
	χ^2/ν	$21/14$	$13/14$		
$l = 6$	c_0 (fm)	5.9083 ± 0.0643	5.8748 ± 0.0561	$+0.57$	$+0.6$
	z (fm)	2.7880 ± 0.0835	2.8009 ± 0.0825	-0.46	-0.2
	w	0.0381 [a]	0.0315 [a]		
	β_2	0.6130 [a]	0.6139 [a]		
	β_4	0.1932 [a]	0.1944 [a]		
	β_6	0.0490 ± 0.0048	0.0504 ± 0.0047	-2.78	-0.3
	$R_{\text{tr}}|_6$ (fm)	8.0586 ± 0.1106	8.0382 ± 0.1070	$+0.25$	$+0.2$
	$B(E6)$ (e^2b^6)	0.0106 ± 0.0021	0.0103 ± 0.0019	$+2.91$	$+0.2$
	χ^2/ν	$7/12$	$6/12$		

[a]Not varied during fit.

in the analysis produced parameter changes between 0.1 and 1.3 standard deviations. It is not surprising that the SDMG shape yielded better fits than the SDF shape in view of previously obtained results[18] for the nearby spherical nuclei ^{138}Ba and ^{142}Nd. Fits to elastic scattering from these nuclei displayed a clear preference for the faster decrease in density at large radius provided by the e^{-r^2/z^2} dependence of the modified Gaussian shape.

Analysis of the data using a Fourier-Bessel expansion for the transition charge densities permits quantitative examination, in coordinate space, of the effect of the inclusion of coupled-channel corrections in the analysis without the restrictions introduced by the assumption of a simple model for the nuclear charge densities. The results of such an analysis for the ^{152}Sm high-energy data (following the procedures outlined in Sec. III C above) are shown in Table IV. The transition charge densities obtained from the coupled-channel fits are shown in Fig. 4, together with those obtained by SDMG model fits to the data. As

TABLE IV. Saclay 251.5 MeV ^{152}Sm data: Fourier-Bessel fits ($R = 11$ fm for all fits).

Parameter	DWBA	CC $l=0$	DWBA	CC $l=2$
a_1	0.051 34 ± 0.000 08	0.051 33 ± 0.000 08	0.019 67 ± 0.000 46	0.019 83 ± 0.000 45
a_2	0.054 56 ± 0.000 33	0.054 70 ± 0.000 33	0.014 36 ± 0.000 65	0.014 12 ± 0.000 65
a_3	−0.030 12 ± 0.000 79	−0.029 77 ± 0.000 79	−0.020 36 ± 0.000 36	−0.020 55 ± 0.000 36
a_4	−0.029 91 ± 0.000 63	−0.029 83 ± 0.000 63	−0.005 67 ± 0.000 71	−0.005 40 ± 0.000 72
a_5	0.016 92 ± 0.000 62	0.016 81 ± 0.000 62	0.013 20 ± 0.000 58	0.013 35 ± 0.000 58
a_6	0.011 34 ± 0.000 87	0.011 09 ± 0.000 88	−0.000 51 ± 0.001 14	−0.000 52 ± 0.001 13
a_7	−0.005 05 ± 0.000 79	−0.004 95 ± 0.000 79	−0.006 96 ± 0.002 31	−0.006 91 ± 0.002 34
a_8	−0.005 53 ± 0.002 59	−0.005 60 ± 0.002 60	−0.000 47 ± 0.003 00	−0.000 44 ± 0.003 01
a_9	0.002 14 ± 0.001 76	0.002 04 ± 0.001 78	0.003 30 [a]	0.003 35 [a]
a_{10}	0.000 43 [a]	0.000 48 [a]	−0.001 62 [a]	−0.001 58 [a]
a_{11}	−0.000 28 [a]	−0.000 29 [a]		
$R_{tr}\|_l$ (fm)	5.011 06 ± 0.015 95	5.012 91 ± 0.015 94	6.703 7 ± 0.235 0	6.745 2 ± 0.225 4
$B(El)(e^2b^l)$			3.292 ± 0.483	3.417 ± 0.488
χ^2/ν	7/19	7/19	11/20	11/20
		$l=4$		$l=6$
a_1	0.011 20 ± 0.000 37	0.011 18 ± 0.000 38	0.004 27 ± 0.000 36	0.004 37 ± 0.000 37
a_2	0.007 66 ± 0.000 34	0.007 96 ± 0.000 34	0.001 90 ± 0.000 38	0.002 17 ± 0.000 37
a_3	−0.008 42 ± 0.000 41	−0.008 01 ± 0.000 42	−0.004 40 ± 0.000 44	−0.004 17 ± 0.000 43
a_4	−0.002 06 ± 0.000 61	−0.002 54 ± 0.000 60	−0.001 73 ± 0.000 75	−0.001 86 ± 0.000 71
a_5	0.006 44 ± 0.000 60	0.006 52 ± 0.000 60	0.003 33 ± 0.000 95	0.003 32 ± 0.000 95
a_6	0.000 75 ± 0.002 10	0.000 16 ± 0.002 08	−0.000 56 ± 0.001 70	−0.000 90 ± 0.001 64
a_7	−0.004 91 ± 0.001 67	−0.004 88 ± 0.001 68	−0.002 15 [a]	−0.001 88 [a]
a_8	0.000 30 [a]	0.000 18 [a]	0.002 05 [a]	0.002 13 [a]
a_9	0.001 61 [a]	0.001 79 [a]		
$R_{tr}\|_l$ (fm)	7.703 9 ± 0.296 8	7.828 1 ± 0.270 4	8.543 2 ± 0.514 6	8.657 7 ± 0.434 5
$B(El)(e^2b^l)$	0.281 9 ± 0.068 9	0.298 6 ± 0.071 4	0.022 9 ± 0.014 3	0.025 8 ± 0.015 0
χ^2/ν	14/17	7/17	5/16	4/16

[a] Not varied in final fit.

one would expect from the χ^2 values, the shapes are in good agreement. The $B(El)$ and transition radii obtained from the Fourier-Bessel analysis are also in excellent agreement with the results obtained by separated model fits to the data. Figure 5 shows the uncertainty $\Delta\rho_l(r)$ in each transition charge density $\rho_l(r)$ as obtained from the Fourier-Bessel analysis. For comparison, the difference in the deduced charge densities due to the inclusion of coupled-channel effects is also shown. The changes in the deduced densities typically lie within the statistical error band obtained from Fourier-Bessel analysis. However, there are clearly regions where coupled-channel effects are comparable to other sources of uncertainty in the charge density. Furthermore, these effects represent systematic rather than statistical errors in the densities. This figure suggests that if other sources of uncertainty are reduced significantly from present levels by improved experimental technique, then coupled-channel corrections could become a dominant source of uncertainty in the interpretation of electron-scattering experiments.

The results of this analysis also clearly indicate the difficulty of distinguishing between dispersive effects and nuclear shape effects in electron-scattering experiments. As can be seen in Table IV, equally good fits were obtained for both the DWBA and the coupled-channel analysis of the ^{152}Sm data, even though the calculated cross sections differed by as much as a factor of 2 in the minima. Consider, for example, the $l=4$ excitation where diffraction minima are observed at 1.2 and 1.75 fm^{-1}. The coupled-channel calculation predicts a filling in of these minima by 20% and 30% respectively as shown in Fig. 2. This additional cross section results primarily in a modification of the a_{42} and a_{44} coefficients in the $l=4$ transition charge density. As can be seen in Fig. 5, the coupled-channel transition charge density differs from the DWBA transition charge density primarily at wavelengths of
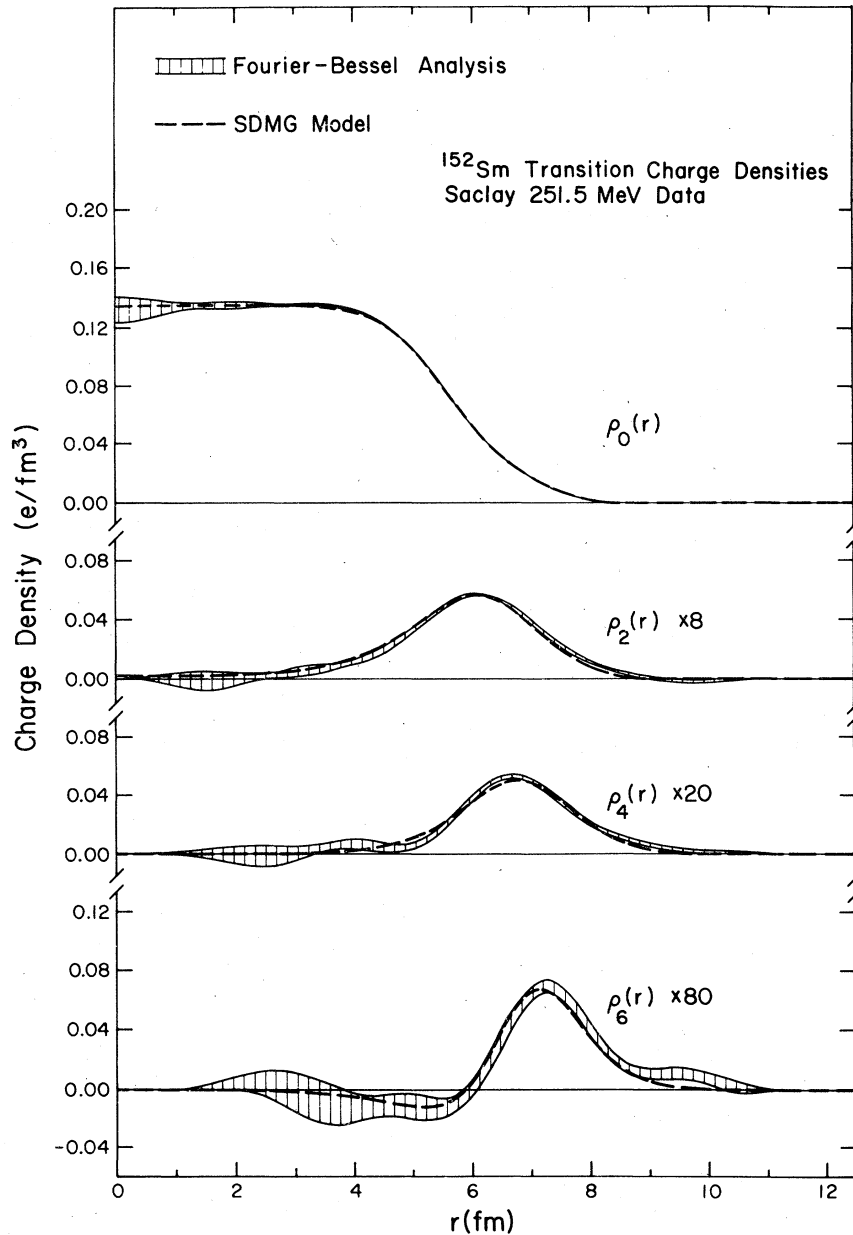
FIG. 4. Best-fit transition charge densities for ^{152}Sm. The solid curves result from the extremes allowed by the Fourier-Bessel analysis, while the dashed curves are the results of the SDMG model analysis. Note that the densities plotted are twice the density defined in Eq. (1) for ρ_0 (r) and $1/\sqrt{\pi}$ times the densities defined in Eq. (1) for the other $\rho_l(r)$.

approximately 6 and 11 fm. These are precisely the wavelengths determined from the scattering observed in the minima. It is probable that no definitive indication can be obtained regarding the presence of dispersive effects in electron-scattering data until it is possible to obtain data with sufficiently high accuracy at several beam energies and overlapping momentum transfers, and to demonstrate that no single static shape can fit all

of the data simultaneously.

The transition charge densities obtained from Fourier-Bessel analysis of the data can be combined using Eq. (1) to determine the intrinsic nuclear shape under the assumption of rigid rotation. The resulting shape for ^{152}Sm is shown in Fig. 6 together with the shapes obtained from the DF and SDMG model fits. The contours at 10%, 50%, and 90% of the central density as obtained in
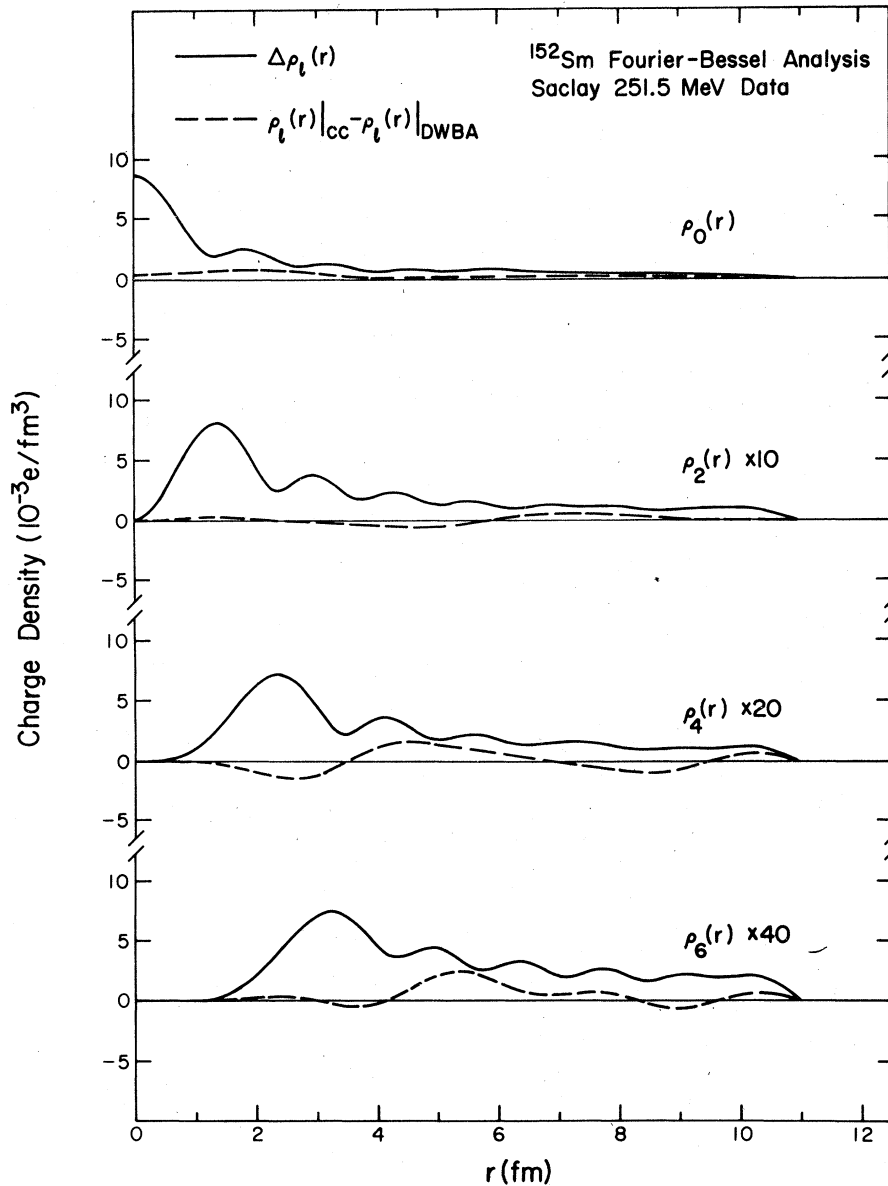
FIG. 5. The solid curves are the uncertainties in the transition charge densities for ^{152}Sm as obtained from the Fourier-Bessel analysis of the Saclay high-energy data. The dashed curves are the changes in these transition charge densities due to the inclusion of coupled-channel effects in the analysis. Note that the densities plotted are twice the density defined in Eq. (1) for ρ_0 (r), and $1/\sqrt{\pi}$ times the densities defined in Eq. (1) for the other ρ_l (r).

all three fits are essentially identical. In the SDMG fit we also observe lobes in the charge density. The deformed Fermi shape (with $w = 0$, as was the case in this analysis) does not have the freedom to produce such lobes, which explains why none are observed in this fit. It is particularly interesting to note that the lobes persist in the Fourier-Bessel analysis result. They are probably a real feature of the ^{152}Sm charge density. However, the modulations of the 100% den-

sity contour in the Fourier-Bessel analysis result are probably not real. In this region the slope of the density is quite low, and the precise shape of the contour results from small oscillations of the various transition densities due to the finite range of momentum transfer available. A smooth curve could be drawn within the error band associated with the location of this 100% density contour. The contours shown are taken from the coupled-channel fits. The associated DWBA results
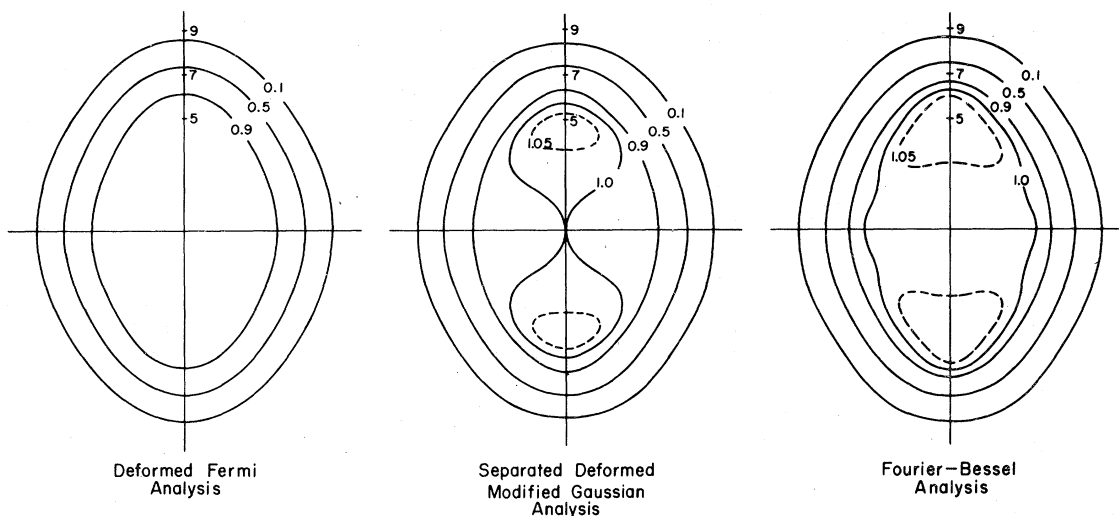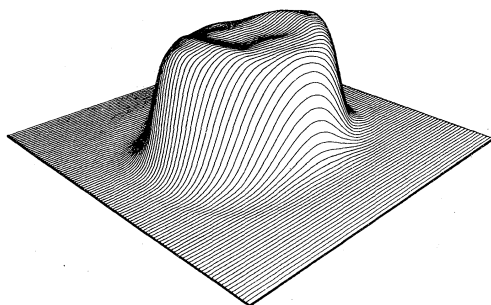
^{152}Sm INTRINSIC SHAPES

Deformed Fermi
Analysis

Separated Deformed
Modified Gaussian
Analysis

Fourier-Bessel
Analysis

FIG. 6. Constant charge density contours for ^{152}Sm as obtained from three different analyses of the data (see text).

differ primarily in the location of the 100% and 105% contours. These differences are modest, and lie within the error band associated with the location of each contour. The difference between the DWBA and coupled-channel results for the 10%, 50%, and 90% contours cannot be seen on a plot of this size. A perspective view of the ^{152}Sm density, as obtained from the Fourier-Bessel analysis, is shown in Fig. 7. It clearly displays the lobes in the density suggested by the contour plots as well as two smaller lobes which give rise to the observed fluctuations in the 100% density contour. A similar plot for the intrinsic shape as obtained

^{152}Sm Intrinsic Shape
Fourier-Bessel Analysis

FIG. 7. A perspective view of the ^{152}Sm charge density as obtained from the Fourier-Bessel coupled-channel analysis.

from the DWBA analysis of the data would be indistinguishable from Fig. 7.

B. NBS-MIT low-energy data

We have also applied coupled-channel techniques to the analysis of the original NBS-MIT low-energy measurements[7,19] of electron scattering from ^{152}Sm. In fitting ^{152}Sm data restricted to a region of momentum transfer $q_{eff} < 1$ fm^{-1}, it is necessary to include constraints on the rms radius and the $B(E2)$ in order to extract an intrinsic shape. Following Bertozzi et al.,[7] we rigidly constained the rms radius and $B(E2)$ to the values shown in Table VI, fixed β_6 to the value they used (obtained from an earlier α scattering experiment[20]), and fit the observed scattering using the deformed Fermi distribution. The results of this fit, which are shown in Table V, are in excellent agreement with the shape obtained by Bertozzi et al.[7,19] The deduced shape is insensitive to the choice of β_6: reanalyzing the data using the β_6 obtained from the high-q electron-scattering data resulted in a negligible change in the best-fit parameter set. Figure 8 displays the coupled-channel corrections obtained by ZENITH for this nuclear shape. Reanalysis of the data including these coupled-channel effects result in the second set of parameters listed in Table V, and the best-fit form factors are shown in Fig. 9. The parameter changes due to the inclusion of coupled-channel effects are somewhat larger for this data, probably due to

TABLE V. NBS-MIT low-energy ^{152}Sm data: deformed Fermi distribution fits. The data are from Table II of Ref. 19. The energy of the fourth cross section measurement was corrected to be 76.08 MeV rather than 67.08 MeV.

Parameter	DWBA analysis	Coupled-channel analysis	% dif.	dif./error
c_0 (fm)	5.7920 ± 0.0262	5.7917 ± 0.0264		
z (fm)	0.5868 ± 0.0113	0.5868 ± 0.0114		
β_2	0.2878 ± 0.0015	0.2871 ± 0.0015	$+0.24$	$+0.5$
β_4	0.0697 ± 0.0012	0.0724 ± 0.0013	-3.73	-2.1
β_6	-0.012 [a]	-0.012 [a]		
$\langle r^2 \rangle^{1/2}$ (fm)	5.0922 [a]	5.0922 [a]		
$R_{tr}\vert_2$ (fm)	6.9486 ± 0.0063	6.9524 ± 0.0063	-0.05	-0.6
$R_{tr}\vert_4$ (fm)	7.7512 ± 0.0188	7.7457 ± 0.0190	$+0.07$	$+0.3$
$B(E2)$ (e^2b^2)	3.380 [a]	3.380 [a]		
$B(E4)$ (e^2b^4)	0.1343 ± 0.0028	0.1406 ± 0.0031	-4.48	-2.0
χ_0^2	5.1	4.0		
χ_2^2	3.7	4.2		
χ_4^2	19.4	16.6		
$\chi_{constraints}^2$	0.9	0		
χ_{total}^2	28.3	24.9		
ν	14	14		

[a]Rigidly constrained to values shown during fit.

TABLE VI. ^{152}Sm pseudodata: deformed Fermi distribution fits. The pseudodata were generated using the deformed Fermi shape with c_0=5.7752 fm, z=0.5501 fm, β_2 = 0.2888, β_4 =0.0881, β_6 =0.0168, implying $\langle r^2 \rangle^{1/2}$=5.0316 fm, $R_{tr}\vert_2$ = 6.9067 fm, $R_{tr}\vert_4$=7.6680 fm, $R_{tr}\vert_6$=8.3601 fm, $B(E2)$=3.518 e^2b^2, $B(E4)$ = 0.2101 e^2b^4 and $B(E6)$ = 0.0141 e^2b^6. $\langle r^2 \rangle^{1/2}$ was constrained by adding the rms radius as a data point in the fit, $\langle r^2 \rangle_{const.}^{1/2}$ = 5.085 $\pm$ 0.06 fm.

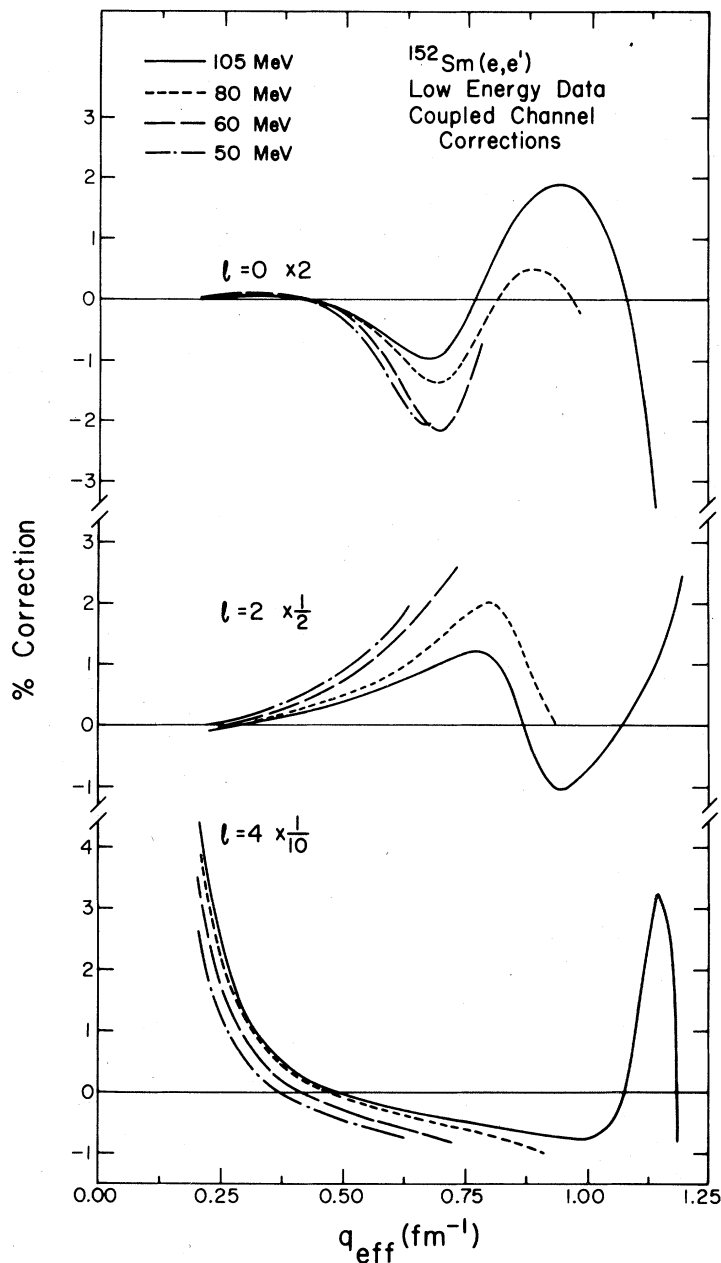| Parameter	DWBA analysis	Coupled-channel analysis	% dif.	dif./error
c_0 (fm)	5.7877 ± 0.0043	5.7778 ± 0.0043	$+0.17$	$+2.3$
z (fm)	0.5489 ± 0.0016	0.5499 ± 0.0016	-0.18	-0.6
β_2	0.2914 ± 0.0013	0.2888 ± 0.0013	$+0.90$	$+2.0$
β_4	0.0897 ± 0.0007	0.0884 ± 0.0006	$+1.47$	$+2.2$
β_6	0.0161 ± 0.0003	0.0166 ± 0.0002	-3.01	-2.5
$\langle r^2 \rangle^{1/2}$ (fm)	5.0412 ± 0.0027	5.0325 ± 0.0027	$+0.17$	$+3.2$
$R_{tr}\vert_2$ (fm)	6.9213 ± 0.0045	6.9078 ± 0.0044	$+0.20$	$+3.1$
$R_{tr}\vert_4$ (fm)	7.6810 ± 0.0059	7.6667 ± 0.0058	$+0.19$	$+2.5$
$R_{tr}\vert_6$ (fm)	8.3823 ± 0.0075	8.3613 ± 0.0073	$+0.25$	$+2.9$
$B(E2)$ (e^2b^2)	3.626 ± 0.030	3.505 ± 0.029	$+3.45$	$+4.2$
$B(E4)$ (e^2b^4)	0.2211 ± 0.0025	0.2100 ± 0.0023	$+5.29$	$+4.8$
$B(E6)$ (e^2b^6)	0.0147 ± 0.0003	0.0140 ± 0.0002	$+5.00$	$+3.5$
χ_0^2	15	14		
χ_2^2	32	18		
χ_4^2	44	19		
χ_6^2	165	14		
$\chi_{constraints}^2$	0.5	0.8		
χ_{total}^2	256	66		
ν	67	67		

FIG. 8. Coupled-channel dispersion correction, in percent, for the $l = 0$, 2, and 4 scattering in ^{152}Sm, as calculated by ZENITH for the lower energies of the NBS-MIT experiment. The correction is defined by Eq. (11).

the fact that a larger fraction of the low-energy data is in the diffraction minimum where the coupled channel effects are greatest.

The Saclay high-energy measurements and the NBS-MIT low-energy measurements are not in agreement on the magnitude of the 4^+ form factor. The high-energy data are approximately 30% high-

er than the low-energy data at the first maximum of the form factor. Dispersive effects, at least in the context of our rotational model calculation, do not explain this discrepancy, and further investigation has not revealed the cause of this disagreement. It should be noted, however, that the recent (α, α') measurement of the Bochum group[21]
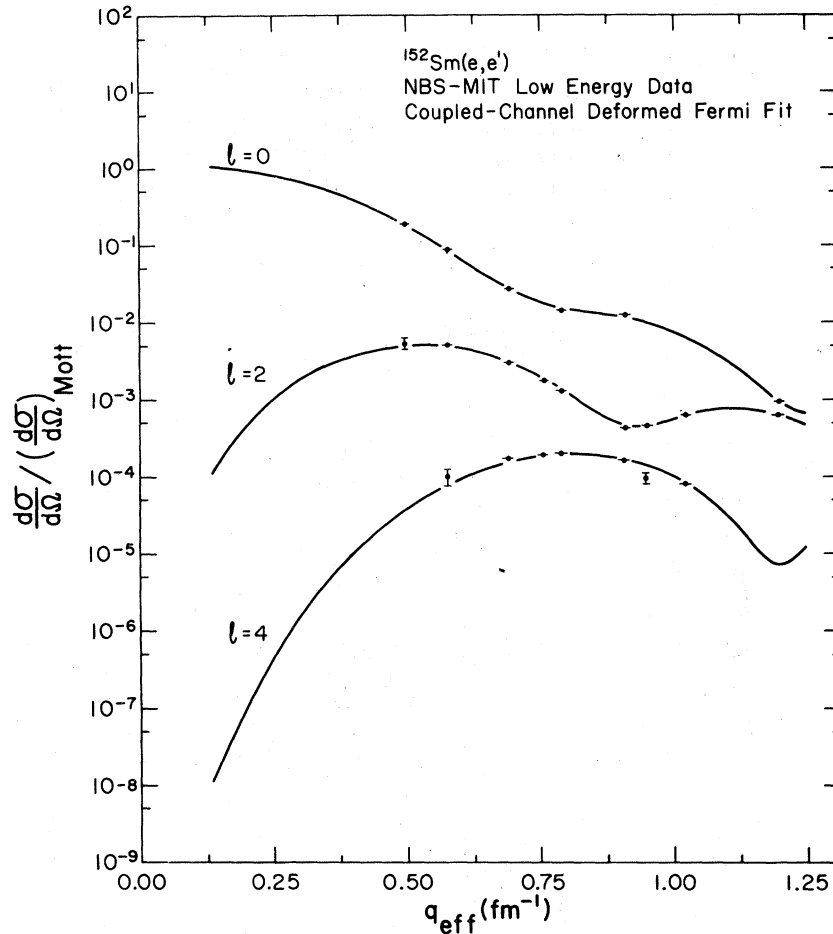
FIG. 9. Experimental form factors (corrected for coupled-channel effects) for elastic (l = 0) and inelastic (l = 2 and 4) scattering from ^{152}Sm as measured in the NBS-MIT low-energy experiment (Ref. 19). The solid curves are based on the best-fit deformed Fermi charge distribution.

yields a value of $0.2144 \pm 0.042e^2b^4$ for $B(E4)$, which is in good agreement with the high-energy result, but disagrees with the low-energy result.

C. High-energy pseudodata

It has been noted above, the inclusion of coupled-channel effects in ^{152}Sm yielded only modest changes in the intrinsic nuclear shape deduced. This lack of effect was attributed to the fact that the uncertainties in the experimental cross sections are similar in magnitude to the coupled-channel corrections. In order to examine the level of experimental accuracy at which coupled-channel corrections would become important in the interpretation of ^{152}Sm (e, e') data, we have analyzed a set of pseudodata with improved accuracy.

This pseudodata was generated at the energy and angle combinations measured in the Saclay experiment by first calculating theoretical cross sections (in DWBA) using an assumed deformed Fermi distribution for the intrinsic nuclear shape. In order to simulate the results of an experimental measurement, these theoretical cross sections were then randomized by multiplying each cross section $\sigma_i(E, \theta_i)$ by a factor $(1 + x_i)$, where the x_i were randomly chosen from a Gaussian distributed set having an average value 0.0 and variance of 0.05. Each cross section was then assigned a statistical uncertainty of 5%. Finally, each of the σ_i was multiplied by a factor $1 + F(E_i, \theta_i)$ to include the effect of coupled channels by inverting the correction of Eq. (12). The data were now representative of a possible experimental measurement in which statistical uncertainties for

TABLE VII. ^{152}Sm pseudodata: separated deformed Fermi distribution fits (see Table VI caption regarding pseudodata).

	Parameter	DWBA analysis	Coupled-channel analysis	% dif.	dif./error
$l=0$	c_0 (fm)	5.8001 ± 0.0291	5.7914 ± 0.0301	$+0.15$	$+0.3$
	z (fm)	0.5333 ± 0.0254	0.5413 ± 0.0265	$+1.48$	$+0.3$
	β_2	0.3112 ± 0.0290	0.3039 ± 0.0315	$+2.40$	$+0.2$
	β_4	0.0881[a]	0.0881[a]		
	β_6	0.0168[a]	0.0168[a]		
	$\langle r^2 \rangle^{1/2}$ (fm)	5.0424 ± 0.0090	5.0415 ± 0.0087	$+0.02$	$+0.1$
	χ^2/ν	$15/16$	$11/16$		
$l=2$	c_0 (fm)	5.7749 ± 0.0075	5.7845 ± 0.0074	$+0.17$	$+1.3$
	z (fm)	0.5429 ± 0.0036	0.5412 ± 0.0035	$+0.31$	$+0.5$
	β_2	0.2817 ± 0.0029	0.2832 ± 0.0029	$+0.53$	$+0.5$
	β_4	0.0881[a]	0.0881[a]		
	β_6	0.0168[a]	0.0168[a]		
	$R_{\rm tr}\vert_2$ (fm)	6.8815 ± 0.0116	6.8883 ± 0.0115	$+0.10$	$+0.6$
	$B(E2)$ (e^2b^2)	3.322 ± 0.079	3.378 ± 0.080	$+1.66$	$+0.7$
	χ^2/ν	$14/17$	$12/17$		
$l=4$	c_0 (fm)	5.7887 ± 0.0059	5.7681 ± 0.0059	$+0.36$	$+3.5$
	z (fm)	0.5477 ± 0.0030	0.5497 ± 0.0031	-0.36	$+0.7$
	β_2	0.2914[a]	0.2888[a]		
	β_4	0.0889 ± 0.0012	0.0874 ± 0.0012	$+1.72$	$+1.3$
	β_6	0.0161[a]	0.0166[a]		
	$R_{\rm tr}\vert_4$ (fm)	7.6786 ± 0.0108	7.6592 ± 0.0110	$+0.25$	$+1.8$
	$B(E4)$ (e^2b^4)	0.2182 ± 0.0052	0.2055 ± 0.0049	$+6.18$	$+2.6$
	χ^2/ν	$43/14$	$17/14$		
$l=6$	c_0 (fm)	5.7965 ± 0.0053	5.7770 ± 0.0049	$+0.34$	$+4.0$
	z (fm)	0.5472 ± 0.0030	0.5505 ± 0.0030	-0.60	-1.1
	β_2	0.2914[a]	0.2888[a]		
	β_4	0.0897[a]	0.0884[a]		
	β_6	0.0162 ± 0.0003	0.0167 ± 0.0003	-3.00	-1.7
	$R_{\rm tr}\vert_6$ (fm)	8.3823 ± 0.0139	8.3650 ± 0.0141	$+0.21$	$+1.2$
	$B(E6)$ (e^2b)	0.0150 ± 0.0003	0.0141 ± 0.0003	$+6.38$	$+3.0$
	χ^2/ν	$163/12$	$14/12$		

[a]Not varied during fit.

all measured cross sections were 5%. It was comparable in accuracy to the Saclay experiment for the $l=0$ and $l=2$ excitation, but represents a fourfold improvement in accuracy for the $l=4$ measurements and a tenfold improvement in accuracy for the $l=6$ measurements. These data were treated in the usual manner—that is, they were first analyzed in DWBA, corrected for coupled-channel effects based on the DWBA best-fit charge density, and then reanalyzed.

The fits obtained for this data using the deformed Fermi distributions are shown in Table VI. The coupled-channel fit is essentially perfect, verifying the procedure used for generating the data set. The neglect of coupled-channel effects results in errors of as much as four standard deviations in the parameters of the charge density deduced from this data. Similar results were obtained using the separated deformed Fermi distribution as shown in Table VII. In this case, parameter differences are less than 1.3 standard deviations for the $l=0$ and $l=2$ analysis, but as much as 3.5 and 4.0 standard deviations for the $l=4$ and $l=6$ analysis, respectively. This result
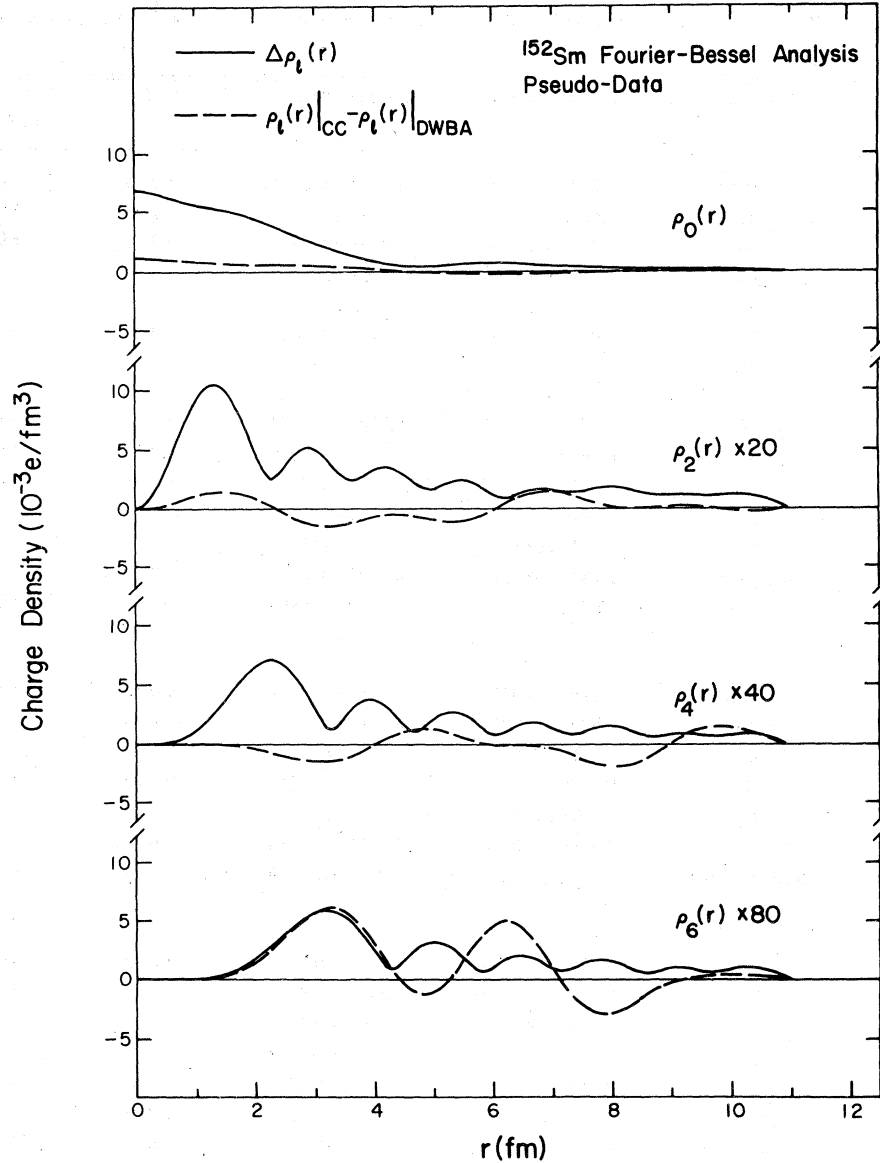
FIG. 10. The solid curves are the uncertainties in the transition charge densities for ^{152}Sm as obtained from the Fourier-Bessel analysis of pseudodata (see text). The dashed curves are the changes in these transition charge densities due to the inclusion of coupled-channel effects in the analysis. Note that the densities plotted are twice the density defined in Eq. (1) for $\rho_0(r)$, and $1/\sqrt{\pi}$ times the densities defined in Eq. (1) for the other $\rho_l(r)$.

may be understood by noting that the coupled-channel corrections, as displayed in Fig. 2, are less than 5% for $l=0$ and $l=2$ scattering, but are as large as 30% for $l=4$ and 100% for $l=6$ scattering. We note also that the SDF model is unable to achieve a good fit to the $l=4$ and $l=6$ data, particularly in the diffraction minima where the coupled-channel effects are largest. Even the Fourier-Bessel analysis, which has considerably more flexible transition charge densities, cannot reproduce the form factor in DWBA, as can be

seen in Table VIII. In Fig. 10 we plot, for the Fourier-Bessel analysis of the pseudodata, the uncertainty in each transition charge density compared to the difference between the coupled-channel and DWBA results. The $l=0$ and $l=2$ plots are similar to those obtained for the Saclay data, presumably because the Saclay data already had cross section uncertainties of order 5% for these states. However, for the $l=4$ and $l=6$ data we now see that the error due to the omission of coupled-channel effects in the analysis is com-

TABLE VIII. ^{152}Sm pseudodata: Fourier-Bessel fits (see Table VI caption regarding pseudodata. $R = 11.0$ fm for all fits).

Parameter	DWBA	CC	DWBA	CC
		$l = 0$		$l = 2$
a_1	0.05105 ± 0.00020	0.05106 ± 0.00020	0.01873 ± 0.00030	0.01882 ± 0.00029
a_2	0.05366 ± 0.00133	0.05384 ± 0.00133	0.01256 ± 0.00053	0.01237 ± 0.00053
a_3	-0.02802 ± 0.00157	-0.02770 ± 0.00158	-0.02100 ± 0.00031	-0.02128 ± 0.00030
a_4	-0.02928 ± 0.00072	-0.02931 ± 0.00072	-0.00682 ± 0.00040	-0.00658 ± 0.00040
a_5	0.01544 ± 0.00052	0.01534 ± 0.00052	0.01547 ± 0.00021	0.01563 ± 0.00021
a_6	0.01297 ± 0.00040	0.01291 ± 0.00040	0.00106 ± 0.00033	0.00087 ± 0.00033
a_7	-0.00660 ± 0.00027	-0.00649 ± 0.00027	-0.00819 ± 0.00092	-0.00840 ± 0.00091
a_8	-0.00460 ± 0.00102	-0.00447 ± 0.00101	0.00126 ± 0.00236	0.00152 ± 0.00230
a_9	0.00290 ± 0.00121	0.00291 ± 0.00121	0.00175 [a]	0.00147 [a]
a_{10}	-0.00013 [a]	-0.00011 [a]	-0.00209 [a]	-0.00213 [a]
a_{11}	-0.00012 [a]	-0.00015 [a]		
$R_{tr}|_l$ (fm)	5.05305 ± 0.02873	5.05256 ± 0.02854	6.8041 ± 0.1444	6.8098 ± 0.1409
$B(El)(e^2b^l)$			3.152 ± 0.297	3.198 ± 0.295
χ^2/ν	$16/19$	$12/19$	$14/20$	$11/20$
		$l = 4$		$l = 6$
a_1	0.01014 ± 0.00016	0.01012 ± 0.00016	0.00391 ± 0.00006	0.00387 ± 0.00007
a_2	0.00817 ± 0.00016	0.00811 ± 0.00016	0.00204 ± 0.00005	0.00225 ± 0.00005
a_3	-0.00928 ± 0.00013	-0.00891 ± 0.00012	-0.00537 ± 0.00006	-0.00504 ± 0.00005
a_4	-0.00334 ± 0.00014	-0.00384 ± 0.00014	-0.00115 ± 0.00006	-0.00141 ± 0.00005
a_5	0.00785 ± 0.00018	0.00797 ± 0.00017	0.00370 ± 0.00022	0.00389 ± 0.00021
a_6	-0.00033 ± 0.00042	-0.00056 ± 0.00042	-0.00189 ± 0.00068	-0.00122 ± 0.00064
a_7	-0.00552 ± 0.00131	-0.00557 ± 0.00128	-0.00163 [a]	-0.00151 [a]
a_8	0.00089 [a]	0.00116 [a]	0.00242 [a]	0.00228 [a]
a_9	0.00129 [a]	0.00122 [a]		
$R_{tr}|_l$ (fm)	7.4076 ± 0.1605	7.6075 ± 0.1376	8.0020 ± 0.2282	8.0535 ± 0.2265
$B(El)(e^2b^l)$	0.1834 ± 0.0211	0.2040 ± 0.0223	0.0115 ± 0.0021	0.0113 ± 0.0021
χ^2/ν	$37/17$	$13/17$	$150/16$ [b]	$14/16$

[a]Not varied in final fit.
[b]102 of the χ^2 total comes from one data point (60.150°).

parable to experimental uncertainties in the transition charge. The structure observed in these difference charge densities can be understood by arguments identical to those presented in Sec. IV A. for the Saclay data Fourier-Bessel analysis.

We have also generated a second set of pseudodata with $2\frac{1}{2}\%$ average uncertainty. This represents approximately a twofold improvement in accuracy for $l = 0$ and $l = 2$ measurements when compared to the Saclay experiment. For these data, the coupled-channel effects are comparable to experimental uncertainties for the $l = 0$ and $l = 2$ scattering also. It is clear, then, that modern electron-scattering experiments are rapidly approaching the level of accuracy at which coupled-channel effects will no longer be negligible.

V. ANALYSIS OF ^{166}Er DATA

The case of ^{166}Er is particularly interesting from the point of view of coupled-channel effects because this nucleus has a rather small hexadecapole moment. [The $B(E4)$ for ^{166}Er is approximately $\frac{1}{7}$ the value of the $B(E4)$ in ^{152}Sm.] Owing to this fact, the single-step excitation of the $l = 4$ state is suppressed, and the (two-step) sequential excitation of this level is relatively more important. The data analyzed for ^{166}Er were the results obtained by the MIT group for the scattering of electrons of energies between 34.65 and 321.28 MeV. The lower-energy data were obtained in collaboration with the NBS electron-scattering group, and have already been reported.[19] The high-energy

data were obtained in a recently completed experiment at the Bates Linear Accelerator.[6] As the two experiments yielded generally consistent results for the scattering from ^{166}Er, the data were combined for the purpose of this analysis.

Our attempts to fit this data using either a deformed Fermi distribution or a deformed modified Gaussian distribution for the intrinsic shape were unsuccessful, presumably due to the fact that the length parameters for the ^{166}Er transition charge densities are even more disparate than was the case in ^{152}Sm. This can be seen clearly in Tables

IX and X where the best-fit parameter sets for the analysis of these data using the separated deformed Fermi (SDF) and separated deformed modified Gaussian (SDMG) distributions are presented. The coupled-channel corrections to this data, based on the SDMG fit, are shown in Fig. 11. The general features of these corrections, as discussed in Sec. IV A. above, are seen to also apply to the case of ^{166}Er. It is clear, however, that the details of the correction vary from nucleus to nucleus, both in the diffraction minima and outside them. The correction to the ^{166}Er $l = 4$ cross sec-

TABLE IX. MIT and NBS-MIT ^{166}Er data: separated deformed Fermi distribution fit.

	Parameter	DWBA analysis	Coupled-channel analysis	% dif.	dif./error
	c_0 (fm)	5.9838 ± 0.0553	5.9546 ± 0.0587	0.49	0.5
	z (fm)	0.4460 ± 0.0314	0.4562 ± 0.0334	−2.24	−0.3
	w	0.1889 ± 0.0688	0.2262 ± 0.0708	−16.49	−0.5
	β_2	0.4404 ± 0.0108	0.4395 ± 0.0119	0.20	0.1
$l = 0$	β_4	0.0^a	0.0^a		
	β_6	0.0^a	0.0^a		
	$\langle r^2 \rangle^{1/2}$ (fm)	5.2373 ± 0.0162	5.2401 ± 0.0163	−0.05	−0.2
	χ^2/ν	60/26	57/26		
	c_0 (fm)	6.1238 ± 0.0505	6.1016 ± 0.0484	0.36	0.5
	z (fm)	0.5440 ± 0.0100	0.5457 ± 0.0098	−0.31	−0.2
	w	-0.2101 ± 0.0745	-0.1550 ± 0.0756	35.55	0.7
	β_2	0.3408 ± 0.0050	0.3403 ± 0.0049	0.15	0.1
$l = 2$	β_4	0.0^a	0.0^a		
	β_6	0.0^a	0.0^a		
	$R_{tr}\vert_2$ (fm)	6.9702 ± 0.0378	6.9932 ± 0.0359	−0.33	−0.6
	$B(E2)$ (e^2b^2)	5.915 ± 0.198	5.918 ± 0.191	−0.05	0.0
	χ^2/ν	103/26	100/26		
	c_0 (fm)	6.1508 ± 0.0776	5.8795 ± 0.0673	4.61	4.0
	z (fm)	0.6503 ± 0.0071	0.6769 ± 0.0073	−3.93	−3.6
	w	-0.4174 ± 0.1736	-0.0133 ± 0.1729	3038.35	2.3
	β_2	0.3504^a	0.3504^a		
$l = 4$	β_4	0.0042 ± 0.0028	0.0118 ± 0.0028	−64.41	−2.7
	β_6	0.0^a	0.0^a		
	$R_{tr}\vert_4$ (fm)	8.2828 ± 0.2454	8.5403 ± 0.0537	−3.02	−4.8
	$B(E4)$ (e^2b^4)	0.0851 ± 0.0128	0.1029 ± 0.0091	−17.30	−2.0
	χ^2/ν	80/23	62/23		
	c_0 (fm)	5.5358 ± 0.1701	5.4652 ± 0.1931	1.29	0.4
	z (fm)	0.9464 ± 0.0679	0.9510 ± 0.0806	−0.15	0.0
	w	-0.0769 ± 0.4054	-0.0020 ± 0.4547	3745.00	0.2
	β_2	0.6211^a	0.6211^a		
$l = 6$	β_4	0.0276^a	0.0276^a		
	β_6	0.0098 ± 0.0031	0.0112 ± 0.0030	12.50	−0.5
	$R_{tr}\vert_6$ (fm)	10.7179 ± 0.1273	10.7571 ± 0.0708	−0.36	−0.6
	$B(E6)$ (e^2b^6)	0.1125 ± 0.0206	0.1109 ± 0.0274	1.80	0.1
	χ^2/ν	7/8	6/8		

^{a}Not varied during fit.

TABLE X. MIT and NBS-MIT ^{166}Er data: separated deformed modified Gaussian distribution fits.

	Parameter	DWBA analysis	Coupled-channel analysis	% dif.	dif./error
	c_0 (fm)	5.2629 ± 0.0458	5.2360 ± 0.0462	0.51	0.6
	z (fm)	3.0331 ± 0.0296	3.0147 ± 0.0299	0.61	0.6
	w	0.7204 ± 0.0785	0.7315 ± 0.0781	-1.51	-0.0
	β_2	0.4168 ± 0.1778	0.5171 ± 0.1528	-19.40	-0.7
$l=0$	β_4	0^a	0^a		
	β_6	0^a	0^a		
	$\langle r^2 \rangle^{1/2}$ (fm)	5.2551 ± 0.0174	5.2393 ± 0.0164	0.30	1.0
	χ^2/ν	67/27	66/27		
	c_0 (fm)	5.6981 ± 0.0656	5.7100 ± 0.0610	-0.21	-0.2
	z (fm)	2.8274 ± 0.0236	2.8209 ± 0.0229	0.23	0.3
	w	1.0122 ± 0.2103	1.0708 ± 0.2090	-5.47	-0.3
	β_2	0.8584 ± 0.0298	0.8485 ± 0.0277	1.17	0.4
$l=2$	β_4	0^a	0^a		
	β_6	0^a	0^a		
	$R_{tr}|_2$ (fm)	6.9497 ± 0.0217	6.9577 ± 0.0214	-0.11	-0.4
	$B(E2)$ (e^2b^2)	6.101 ± 0.145	6.017 ± 0.141	1.40	0.6
	χ^2/ν	66/27	69/27		
	c_0 (fm)	6.2169 ± 0.1759	6.2973 ± 0.1621	-1.28	-0.5
	z (fm)	2.8500 ± 0.0516	2.8367 ± 0.0365	0.47	0.0
	w	-0.2489 ± 0.4495	-0.3925 ± 0.2627	-36.56	-0.6
	β_2	0.6766 ± 0.0450	0.6146 ± 0.0281	10.09	2.2
$l=4$	β_4	0.0397 ± 0.0052	0.0448 ± 0.0048	-11.38	-1.0
	β_6	0^a	0^a		
	$R_{tr}|_4$ (fm)	8.0038 ± 0.1661	7.8837 ± 0.0887	1.52	1.4
	$B(E4)$ (e^2b^4)	0.0636 ± 0.0117	0.0533 ± 0.0071	19.32	1.5
	χ^2/ν	84/23	48/23		
	c_0 (fm)	6.2488 ± 1.0445	6.0900 ± 1.0539	2.61	0.2
	z (fm)	3.3250 ± 1.6839	3.4138 ± 1.2332	-2.60	-0.1
	w	-0.1961 ± 4.8286	-0.1556 ± 3.9626	26.03	0.0
	β_2	0.8966 ± 1.1358	0.9765 ± 0.8525	-8.18	-0.1
$l=6$	β_4	0.1106 ± 0.2177	0.1027 ± 0.1527	7.69	0.1
	β_6	0.0177 ± 0.0195	0.0186 ± 0.0192	-4.84	-0.1
	$R_{tr}|_6$ (fm)	9.2316 ± 0.5026	9.2983 ± 0.5026	-0.72	-0.1
	$B(E6)$ (e^2b^6)	0.0181 ± 0.0153	0.0179 ± 0.0136	1.12	0.0
	χ^2/ν	16/7	16/7		

^{a}Not varied during fit.

tion, for example, is 300% in the first diffraction minimum while it reached only 20% in the corresponding minimum in ^{152}Sm. It is also clear from Fig. 11 that the corrections depend on both the energy and the effective momentum transfer, a fact which considerably complicated the analysis of data taken at many energies.

Application of these corrections to the data, as outlined in Sec. III C., resulted in the coupled-channel fits shown in Tables IX and X. The coupled-channel best-fit form factors for the SDMG model are shown in Fig. 12. The quality of the fits was only moderately good, with χ^2 per degree of freedom as large as 4. The SDMG model yielded somewhat better fits to the $l=2$ and $l=4$ scattering. As expected, the inclusion of coupled-channel effects had the largest impact on the $l=4$ transition charge density. Parameter changes of 2 to 5 standard deviations were found in the SDF analysis, while changes of 0.3 to 2.2 standard deviations were observed in the SDMG fits to this data. For all other transition charge densities, the parameter changes due to the inclusion of coupled-channel effects were less than one stand-
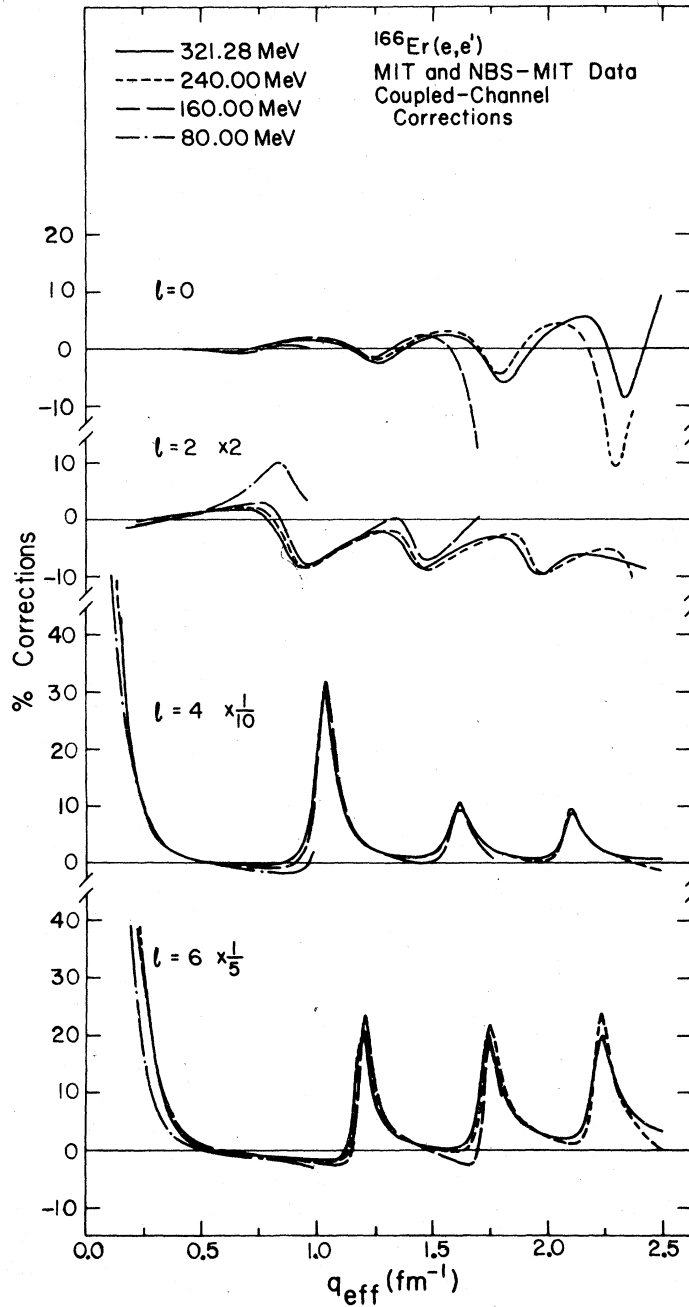
FIG. 11. Coupled-channel dispersion corrections, in percent, for the $l = 0$, 2, 4, and 6 transitions in ^{166}Er, including all couplings shown in Fig. 1(e). The correction is defined by Eq. (11).

ard deviation. In the case of the $l = 4$ transition, the quality of the fits (as measured by χ^2/ν) was significantly improved when coupled-channel effects were included in the analysis. This improvement can be traced directly to the region of the second diffraction minimum. The "filling in" of

this minimum, as predicted by the coupled-channel calculation, is apparently a feature of the measured cross sections.

We have also analyzed the ^{166}Er data using the Fourier-Bessel expansion for the transition charge densities as outlined in Sec. III B. above. The
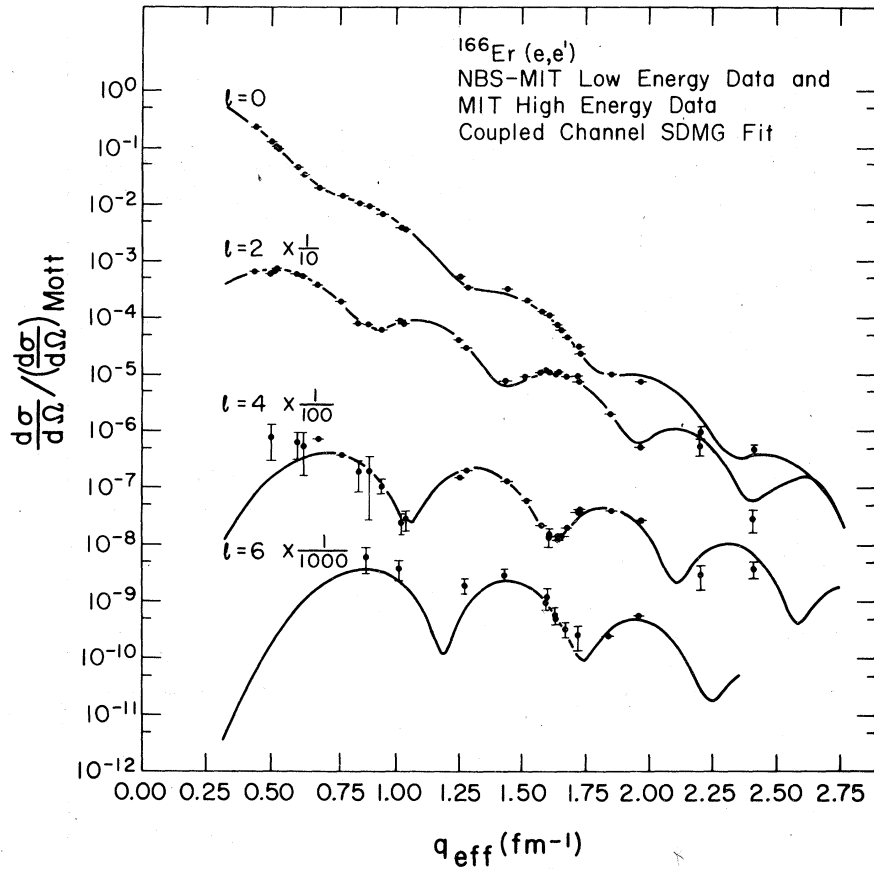
FIG. 12. Experimental form factors (corrected for coupled-channel effects) for elastic $(l = 0)$ and inelastic $(l = 2,$ 4, and 6) scattering in ^{166}Er as measured in the MIT high-energy experiment (Ref. 6) and the NBS-MIT low-energy experiments (Ref. 19). The solid curves are based on the best-fit SDMG charge density.

best-fit coefficients for this data are shown in Table XI for both the DWBA and the coupled-channel analysis. The transition charge densities obtained from the Fourier-Bessel coupled-channel fits are shown in Fig. 13 together with those obtained by SDMG model fits to the data. The agreement between the model analysis and the Fourier-Bessel analysis is not as satisfactory for ^{166}Er as it was for ^{152}Sm. This is not surprising in view of the relatively poor χ^2 values for the SDMG model fits. The most striking differences are those obtained for radii less than 3 fm in the $l = 0$ transition density, where the SDMG analysis predicts a central depression while the Fourier-Bessel analysis results in a central maximum. These differences can be traced directly to the region of the second maximum in the elastic-scattering form factor. The best-fit SDMG model density consistently underestimates the cross section in this region, while the Fourier-Bessel density

yields an excellent fit to the data. If we compare the best-fit Fourier-Bessel coefficients with the coefficient set obtained by analytic expansion of the SDMG model density using Eq. (10), we find that the most significant differences occur in the fourth and fifth coefficients. These coefficients are determined by data at momentum transfers in the region of 1.14 and 1.43 fm^{-1}, respectively, precisely the region of the second maximum. The changes in these two coefficients above explain over 60% of the difference between the central densities $\rho(0)$ as obtained in these two analyses.

The Fourier-Bessel analysis yielded excellent fits to all of the observed scattering data with the exception of the $l = 2$ state, where the lowest χ^2 obtained was over two per degree of freedom. This relatively poor χ^2 is apparently due to an overly optimistic estimate of the cross section uncertainties in the lower-energy NBS-MIT data.[19] Fourier-Bessel fits to the high-energy MIT data
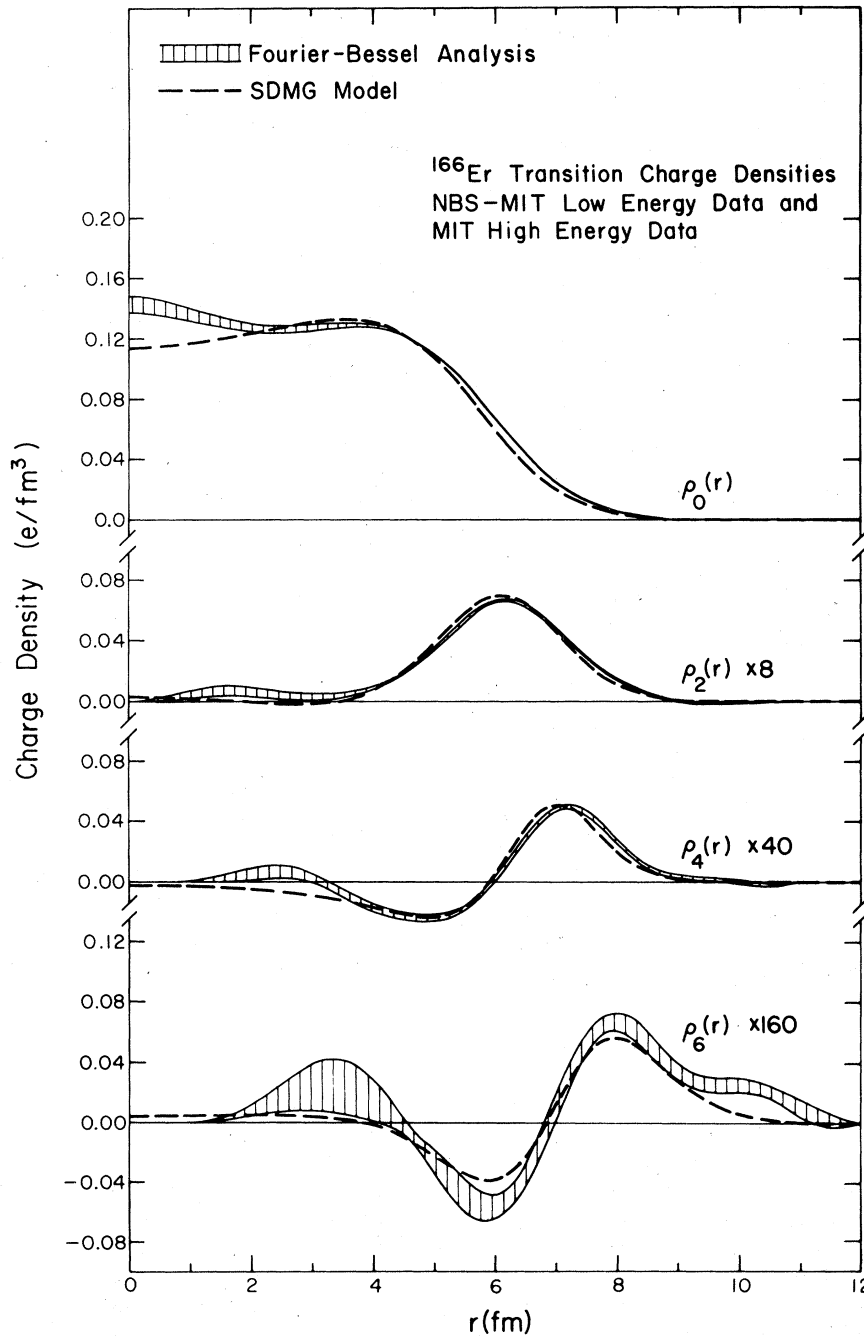
FIG. 13. Best-fit transition charge densities for ^{166}Er. The solid curves result from the extremes allowed by the Fourier-Bessel analysis, while the dashed curved are the results of the SDMG model analysis. Note that the densities plotted are twice the density defined in Eq. (1) for ρ_0 (r), and $1/\sqrt{\pi}$ times the densities defined in Eq. (1) for the other ρ_l (r).

alone yield χ^2/ν values of 16/16, while SDMG model fits to the low-energy data alone yield a χ^2/ν of 22/6. As the energy resolution obtainable in the NBS-MIT experiment was barely adequate to separate the $l=2$ scattering from the elastic scattering (see, for example, Fig. 4 of Ref. 19),

the underestimation of the cross section uncertainties is not surprising. For the $l=4$ scattering, as was the case for the SDMG model analysis, the coupled-channel fit to the data was significantly better than the DWBA fit due to difference between the calculated cross sections in the region of the

TABLE XI. MIT and NBS-MIT [166]Er data: Fourier-Bessel fits. ($R = 11$ fm for $l = 0$, 2, and 4 fits, $R = 12$ fm for $l = 6$ fit).

Parameter	DWBA $l=0$	CC $l=0$	DWBA $l=2$	CC $l=2$
a_1	$0.054\,42 \pm 0.000\,15$	$0.054\,49 \pm 0.000\,15$	$0.024\,60 \pm 0.000\,19$	$0.024\,25 \pm 0.000\,18$
a_2	$0.047\,16 \pm 0.000\,94$	$0.047\,97 \pm 0.000\,94$	$0.014\,77 \pm 0.000\,49$	$0.014\,13 \pm 0.000\,49$
a_3	$-0.038\,65 \pm 0.001\,10$	$-0.037\,59 \pm 0.001\,12$	$-0.026\,03 \pm 0.000\,60$	$-0.026\,18 \pm 0.000\,60$
a_4	$-0.019\,67 \pm 0.001\,39$	$-0.019\,62 \pm 0.001\,38$	$-0.002\,04 \pm 0.001\,09$	$-0.001\,77 \pm 0.001\,09$
a_5	$0.022\,09 \pm 0.000\,83$	$0.022\,16 \pm 0.000\,83$	$0.018\,40 \pm 0.000\,46$	$0.018\,66 \pm 0.000\,47$
a_6	$0.007\,87 \pm 0.000\,56$	$0.007\,89 \pm 0.000\,57$	$-0.001\,95 \pm 0.001\,09$	$-0.002\,14 \pm 0.001\,11$
a_7	$-0.005\,30 \pm 0.000\,51$	$-0.005\,05 \pm 0.000\,50$	$-0.005\,72 \pm 0.001\,13$	$-0.005\,69 \pm 0.001\,16$
a_8	$0.000\,50 \pm 0.000\,64$	$0.000\,25 \pm 0.000\,64$	$0.002\,44 \pm 0.001\,80$	$0.002\,17 \pm 0.001\,86$
a_9	$0.000\,52 \pm 0.000\,82$	$0.001\,30 \pm 0.000\,77$	$0.004\,41$ [a]	$0.004\,56$ [a]
a_{10}	$-0.000\,35$ [a]	$-0.000\,49$ [a]	$-0.002\,41$ [a]	$-0.002\,43$ [a]
a_{11}	$0.000\,12$ [a]	$0.000\,19$ [a]		
$R_{tr}\vert_l$ (fm)	$5.227\,01 \pm 0.020\,28$	$5.222\,20 \pm 0.020\,41$	$6.904\,96 \pm 0.097\,68$	$6.933\,17 \pm 0.097\,35$
$B(El)(e^2b^l)$			5.773 ± 0.331	5.696 ± 0.327
χ^2/ν	$21/27$	$17/27$	$61/28$	$67/28$

	DWBA $l=4$	CC $l=4$	DWBA $l=6$	CC $l=6$
a_1	$0.004\,04 \pm 0.000\,23$	$0.004\,10 \pm 0.000\,23$	$0.002\,27 \pm 0.000\,32$	$0.002\,35 \pm 0.000\,34$
a_2	$-0.000\,66 \pm 0.000\,35$	$-0.000\,35 \pm 0.000\,33$	$-0.000\,87 \pm 0.000\,37$	$-0.000\,56 \pm 0.000\,35$
a_3	$-0.008\,34 \pm 0.000\,21$	$-0.007\,68 \pm 0.000\,17$	$-0.003\,09 \pm 0.000\,17$	$-0.002\,93 \pm 0.000\,16$
a_4	$0.003\,23 \pm 0.000\,20$	$0.002\,17 \pm 0.000\,18$	$0.000\,07 \pm 0.000\,17$	$-0.000\,06 \pm 0.000\,15$
a_5	$0.004\,89 \pm 0.000\,33$	$0.004\,91 \pm 0.000\,29$	$0.002\,82 \pm 0.000\,34$	$0.002\,86 \pm 0.000\,30$
a_6	$-0.001\,33 \pm 0.000\,88$	$-0.002\,29 \pm 0.000\,65$	$-0.000\,27 \pm 0.001\,04$	$0.000\,71 \pm 0.001\,14$
a_7	$-0.002\,28 \pm 0.001\,02$	$-0.000\,28 \pm 0.000\,92$	$-0.000\,86$ [a]	$-0.001\,15$ [a]
a_8	$0.002\,50$ [a]	$0.002\,35$ [a]	$0.001\,03$ [a]	$0.001\,04$ [a]
a_9	$-0.001\,64$ [a]	$-0.001\,43$ [a]		
$R_{tr}\vert_l$ (fm)	$5.453\,13 \pm 1.915\,04$	$7.488\,90 \pm 0.529\,02$	$10.009\,18 \pm 0.237\,11$	$9.788\,35 \pm 0.344\,82$
$B(El)$ (e^2b^l)	$0.019\,42 \pm 0.011\,96$	$0.041\,35 \pm 0.016\,25$	$0.084\,65 \pm 0.039\,11$	$0.069\,40 \pm 0.037\,33$
χ^2/ν	$58/26$	$35/26$	$7/12$	$5/12$

[a]Not varied in final fit.

second minimum.

The agreement between the model fits and the Fourier-Bessel fits for the integral quantities describing the transition charge densities was reasonable with two exceptions; the SDF fit to the $l=4$ transition and the SDMG fit to the $l=6$ transition. The quality of the fits in both of these cases was significantly worse than the quality of the fits obtained by other analyses, and these two fits should probably be discarded. The Fourier-Bessel analysis results for the $B(E2)$ and $B(E4)$

were also in good agreement with the values of $(5.9146 \pm 0.0243)e^2b^2$ and $(0.05856 \pm 0.0348)e^2b^4$ obtained by a recent Coulomb excitation experiment.[21] In Fig. 14 we show the uncertainty $\Delta\rho_l(r)$ in each of the transition charge densities $\rho_l(r)$ as obtained from Fourier-Bessel analysis. For comparison, the differences in the deduced densities due to the inclusion of coupled-channel effects are also shown. For the [152]Sm analysis, these density changes were always bounded by the statistical uncertainty in the experimental data. In contrast,

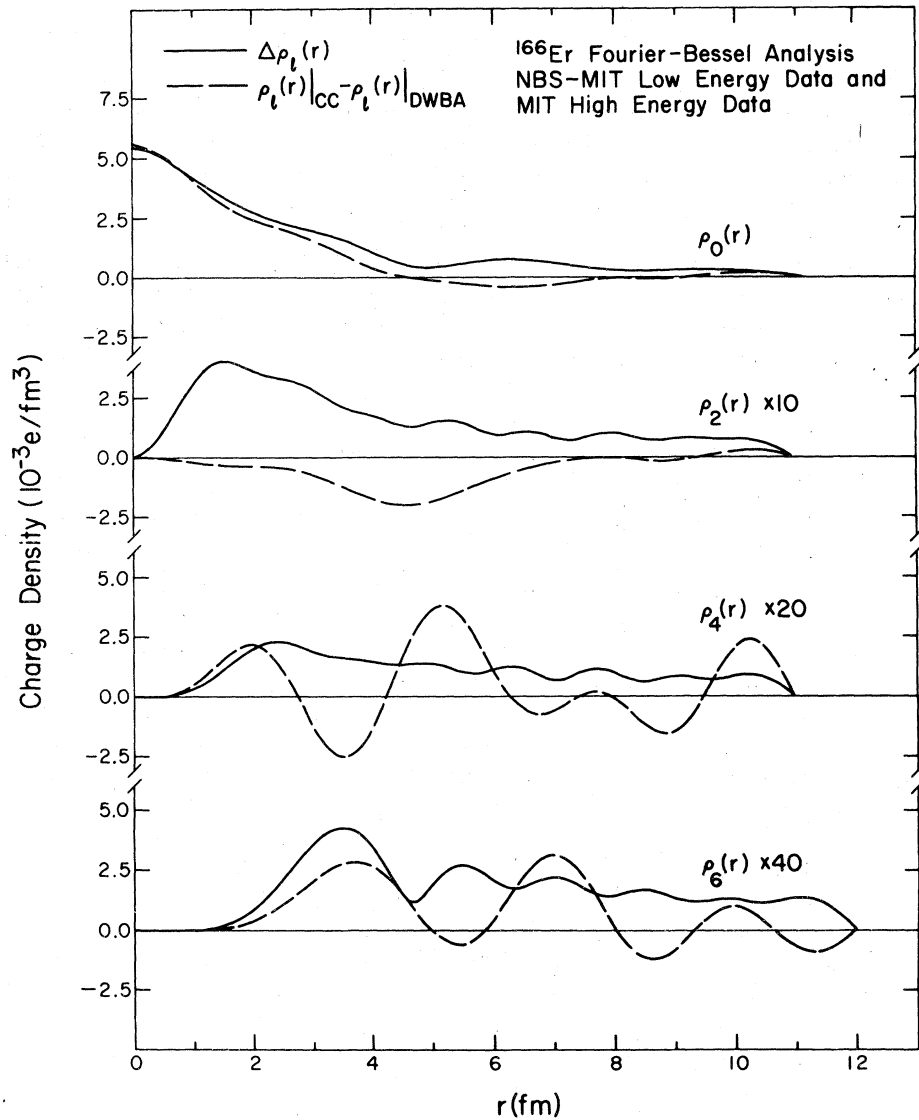FIG. 14. The solid curves are the uncertainties in the transition charge densities for [166]Er as obtained from the Fourier-Bessel Analysis of the MIT high-energy data and the NBS-MIT low-energy data. The dashed curves are the changes in these transition charge densities due to the inclusion of coupled-channel effects in the analysis. Note that the densities plotted are twice the density defined in Eq. (1) for ρ_0 (r), and $1\sqrt{\pi}$ times the densities defined in Eq. (1) for the other $\rho_l(r)$.

for the case of [166]Er these density changes are typically comparable to the experimental uncertainties, and even exceed the experimental uncertainty for significant portions of the $l=4$ and $l=6$ transition densities. As was the case for [152]Sm, we note that the coupled-channel and DWBA transition densities for [166]Er differ primarily at wavelengths corresponding to the diffraction minima. This can be seen both in Fig. 14 and in the coefficient changes in Table XI. It is clear from these results that coupled-channel effects are as important as other sources of uncertainty in the

detailed analysis of electron-scattering data for [166]Er.

In Fig. 15 we show the intrinsic shape for [166]Er obtained from the coupled-channel Fourier-Bessel analysis of the data by combining the transition charge densities under the assumption of rigid rotation by using Eq. (1). Also shown are the shapes obtained using the SDF and SDMG model fits. The contours at 10% and 50% of the central density agree among the fits. All three fits also generate lobes in the density, although the details of these lobes differ significantly among the an-
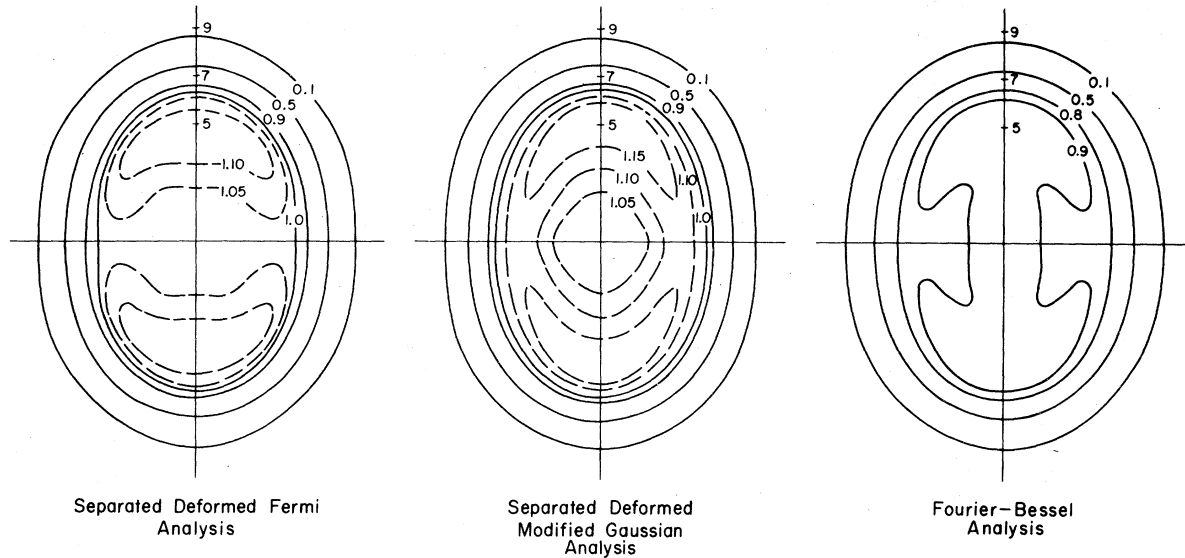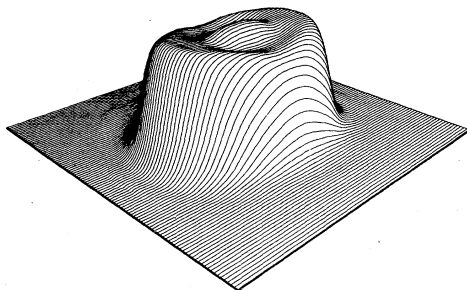
^{166}Er INTRINSIC SHAPES

Separated Deformed Fermi	Separated Deformed	Fourier—Bessel
Analysis	Modified Gaussian	Analysis
	Analysis	

FIG. 15. Constant charge density contours for ^{166}Er as obtained from three different analysis of the data (see text).

alyses. Given the relative quality of the fits to the data, the Fourier-Bessel analysis results are the most reliable. As was the case for ^{152}Sm, the contours obtained from the DWBA analysis of the ^{166}Er data agree with the coupled-channel analysis contours, except in the interior region of the nucleus where the slope of the density is quite low and the location of the contours is sensitive to small changes in the density. Figure 16 shows a perspective view of the ^{166}Er density as obtained

^{166}Er Intrinsic Shape
Fourier—Bessel Analysis

FIG. 16. A perspective view of the ^{166}Er charge density as obtained from the Fourier-Bessel coupled-channel analysis.

from the Fourier-Bessel fit. Both the central maximum and the lobes in the density are clearly visible. A similar plot of the density obtained from the DWBA analysis would be indistinguishable from Fig. 16.

VI. CONCLUSIONS

Dispersion corrections arising from intermediate states in the ground-state rotational band have been calculated for elastic and inelastic electron scattering from ^{152}Sm and ^{166}Er using the coupled-channel computer code ZENITH. These corrections were found to be small (of order 5–10 %) for the $l = 0$ and $l = 2$ scattering, but were considerably larger for $l = 4$ and $l = 6$ scattering where sequential excitations of lower multipolarity can occur. The details of the momentum transfer and energy dependence of these corrections were found to vary significantly between these nuclei, indicating a sensitivity to the details of the transition charge densities involved. Inclusion of these higher-order effects in the analysis of the recent Saclay and MIT experiments was found to affect the extracted transition charge densities at a level comparable to other sources of uncertainty. The errors in the deduced densities due to the neglect of coupled-channel effects were found to occur primarily at wavelengths associated with scatter-

ing in the diffraction minima where the coupled-channel effects are largest. It is clear from our results that an understanding of dispersive processes is important in the detailed interpretation of modern electron-scattering experiments in terms of nuclear transition charge densities. It must be noted, however, that dispersive effects (at least in the context of our calculation) are much smaller than the discrepancies which currently exist between electron-scattering experiments and the predictions of the best available microscopic theories for deformed nuclei.[22]

*Work supported in part by the National Science Foundation under Grants Nos. NSF PHY75-21590 and NSF PHY77-08100.

[1] For a summary of work on this topic, see, for example H. Uberall, *Electron Scattering from Complex Nuclei* (Academic, New York, 1971), Part B, pp. 757–765, and references therein.

[2] R. L. Mercer and D. G. Ravenhall, Phys. Rev. C 10, 2002 (1974).

[3] R. L. Mercer, Phys. Rev. C 15, 1786 (1977).

[4] D. G. Ravenhall and R. L. Mercer, Phys. Rev. C 13, 2324 (1976).

[5] A. Nakada *et al.*, Phys. Rev. Lett. 38, 584 (1977).

[6] C. Creswell *et al.* (unpublished).

[7] W. Bertozzi *et al.*, Phys. Rev. Lett. 28, 1711 (1972).

[8] C. W. deJager (unpublished).

[9] P. R. Bevington, *Data Reduction and Error Analysis for the Physical Sciences* (McGraw-Hill, New York, 1969), Chap. 11.

[10] J. Heisenberg (unpublished).

[11] I. Sick, Phys. Lett. 44B, 62 (1973).

[12] B. Dreher *et al.*, Nucl. Phys. A235, 219 (1974).

[13] H. Rothhaas *et al.*, Phys. Lett. 51B, 23 (1974).

[14] J. L. Friar and J. W. Negele, Nucl. Phys. A212, 93 (1973).

[15] J. Borysowicz and J. H. Hetherington, Phys. Rev. C 7, 2293 (1973).

[16] R. Neuhausen, Nucl. Phys. A282, 125 (1977).

[17] J. L. Friar and J. W. Negele, Adv. Nucl. Phys. 8, 219 (1975); and references therein.

[18] J. Heisenberg *et al.*, in *Topics in Modern Physics: Tribute to E. U. Condon*, edited by W. E. Brittin and H. Odabasi (Adam Hilger, London, 1970), p. 169.

[19] T. Cooper *et al.*, Phys. Rev. C 13, 1083 (1976).

[20] D. L. Hendrie, Phys. Rev. Lett. 36, 571 (1973); D. L. Hendrie *et al.*, Phys. Lett. 26B, 127 (1968).

[21] H. Fischer *et al.*, Phys. Rev. C 15, 921 (1977).

[22] W. Bertozzi, Proceedings of the International Conference on Nuclear Structure, Tokyo, 1977, edited by T. Marumori [J. Phys. Soc. Jpn. Suppl. 44, 173 (1978)].